Selection of Single Domain Anti-Transferrin Receptor Antibodies for Blood-Brain Barrier Transcytosis Using a Neurotensin Based Assay and Histological Assessment of Target Engagement in a Mouse Model of Alzheimer's Disease-Related Amyloid-Beta Pathology

Authors: Shiran Su[1,2], Thomas J. Esparza[1,3,4], & David L. Brody[1,2,3,5*]

[1]Laboratory of Functional and Molecular Imaging, National Institute of Neurological Disorders and Stroke, National Institutes of Health, Bethesda, MD, USA, 20892

[2]Department of Biomedical Engineering, Washington University in St. Louis, St. Louis, MO, USA, 63130

[3]Center for Neuroscience and Regenerative Medicine, Henry M. Jackson Foundation for the Advancement of Military Medicine, Bethesda, MD, USA, 20817

[4]Henry M. Jackson Foundation for the Advancement of Military Medicine, Inc, Bethesda, MD, USA, 20817

[5]Department of Neurology, Uniformed Services University of the Health Sciences, Bethesda, MD, USA, 20814

*Correspondence should be addressed to david.brody@nih.gov or david.brody@usuhs.edu

Abstract

Background: The blood-brain barrier (BBB) presents a major obstacle in developing specific diagnostic imaging agents for many neurological disorders. In this study we aimed to generate single domain anti-mouse transferrin receptor antibodies (anti-mTfR VHHs) to mediate BBB transcytosis as components of novel MRI molecular contrast imaging agents.

Methods: Anti-mTfR VHHs were produced by immunizing a llama with mTfR, generation of a VHH phage display library, immunopanning, and *in vitro* characterization of candidates. Site directed mutagenesis was used to generate additional variants. VHH fusions with neurotensin (NT) allowed rapid, hypothermia-based screening for VHH-mediated BBB transcytosis in wild-type mice. One anti-mTfR VHH variant was fused with an anti-amyloid-beta (Aβ) VHH dimer and labeled with fluorescent dye for direct assessment of *in vivo* target engagement in a mouse model of AD-related Aβ plaque pathology.

Results: An anti-mTfR VHH called M1 and variants had binding affinities to mTfR of <1nM to 1.52nM. The affinity of the VHH binding to mTfR correlated with the efficiency of the VHH-NT induced hypothermia effects after intravenous injection of 600 nmol/kg body weight, ranging from undetectable for nonbinding mutants to -6°C for the best mutants. The anti-mTfR VHH variant $M1_{P96H}$ with the strongest hypothermia effect was fused to the anti-Aβ VHH dimer and labeled with Alexa647; the dye-labeled VHH fusion construct still bound both mTfR and Aβ plaques. However, after intravenous injection at 600 nmol/kg body weight into APP/PS1 transgenic mice, there was no detectible labeling of plaques above control levels. Thus, NT-induced hypothermia did not correlate with direct target engagement in cortex.

Conclusions: There was a surprising dissociation between NT-induced hypothermia, presumably mediated by hypothalamus, and direct engagement with Aβ-plaques in cortex. Alternative methods to assess anti-mTfR VHH BBB transcytosis will need to be developed for anti-mTfR VHH screening and the development of novel MRI molecular contrast agents.

Keywords

Singlet domain antibodies, Blood brain barrier, receptor-mediated transcytosis, transferrin receptor, mouse models, Amyloid-β, Alzheimer's Disease, target engagement, neurotensin

Background

45 Alzheimer's disease (AD) is one of the most important causes of dementia in the elderly[1]. About 6.2
46 million Americans are living with AD, and it's predicted that the number will increase to 13.8 million by
47 2050 [2]. With no effective therapies to cure or inhibit significant AD symptom progression[3], AD
48 severely decreases patients' quality of life and creates an enormous burden on the health care system
49 and society [1, 4]. Currently, clinical AD diagnosis is based on cognition and the relative impact of
50 impairments on daily activities [5]. However, multiple neurodegenerative and vascular pathologies can
51 coexist and produce cognitive and behavioral symptoms which could overlap with each other [6]. This
52 makes it difficult to accurately identify pathology based solely on clinical symptoms. The accuracy of
53 clinical diagnosis of AD at the National Institute of Aging and National Institute of Aging sponsored AD
54 centers varies depending on the clinical and neuropathologic criteria used [7]. The sensitivity of AD
55 diagnosis ranges from 70.9% to 87.3%, whereas specificity ranges from 44.3% to 70.8%, which need to
56 be improved. AD has a very long prodrome stage before clinically observable symptoms [8]. Early
57 diagnosis is preferred to help with early intervention and the development of preventive therapeutics to
58 slow AD development [5]. Detection of patients in the preclinical stages of AD can also help to provide
59 diagnostic information, monitor disease progression, and even monitor the effect of newly developed
60 treatment methods. Imaging methods including MRI and PET have been developed to aid the diagnosis
61 of AD [9, 10]. However, PET imaging for AD provides limited resolution and requires radiation exposure.
62 Structural MRI lacks specificity and does not allow direct visualization of Aβ or tau, the histological
63 hallmarks of AD. There is an unmet need for developing methods like molecular contrast MRI which
64 have better resolution than PET and better specificity than structural MRI imaging.

65

66 The blood-brain barrier (BBB) represents a significant obstacle in delivering diagnostic and therapeutic
67 agents to the central nervous system (CNS), preventing uptake of more than 98% of potential
68 neurotherapeutics to brain [11-14]. The BBB consists of endothelial cells held together by tight junctions

69 which hinder paracellular passage. Most molecules do not transfer from blood to brain through the BBB,
70 which protects the brain from toxicity and maintains brain homeostasis. Several methods have been
71 developed to improve the transport of diagnostic and therapeutic agents into the CNS. For instance, the
72 BBB may be temporarily opened by administration of hypertonic agents or focused ultrasound.
73 Alternatively, very high doses of an agent can be given so that even if a small fraction enters the brain
74 the desired effect will be achieved. In some cases, direct injection of agents into the cerebrospinal fluid
75 can be employed [14]. However, these methods are invasive and have a risk of causing infection,
76 toxicity, and neurological dysfunction [13, 14].
77
78 BBB crossing based on receptor mediated transcytosis (RMT) is potentially especially promising. The use
79 of protein shuttles has the potential to facilitate the transport of therapeutic agents across the BBB
80 using specific endogenous receptor systems. Candidate receptor systems including transferrin receptors
81 (TfR), low-density lipoprotein receptors, insulin receptors and neuropeptide receptors are highly
82 expressed on the BBB where they mediate receptor-mediated transcytosis [13]. Among the different
83 receptors, TfR has been widely used for transporting macromolecules across the BBB [15, 16]. Based on
84 the study of Yu et al., there is a nonlinear relationship between an antibody's affinity for TfR and its
85 uptake in brain. At tracer doses, antibodies with higher affinity to TfR have higher uptake into the brain,
86 while at therapeutic doses, antibodies with lower affinity to brain have higher uptake into the brain [17].
87 The effect of TfR affinity on brain uptake has been confirmed by the study of Wiley et al [18]. Transferrin
88 conjugated gold nanoparticles with high avidity to TfR remain strongly attached to brain endothelial cells
89 and reduced accumulation in brain parenchyma compared with nanoparticles with lower avidity to TfR
90 [18]. Thus, to achieve optimal brain uptake, it is important to optimize anti-TfR concentration and
91 antibody affinity to TfR. Jefferies et al. identified a monoclonal antibody OX-26 specific for transferrin
92 receptors [19]. This antibody was tested and was confirmed to be able to facilitate TfR-mediated

93 transcytosis across BBB [20]. Yu et al. generated a bispecific antibody that binds to TfR for transcytosis
94 and also to the enzyme β-secretase for inhibiting Aβ production[17]. However, the existing anti-TfR
95 antibodies have relatively large size, especially when conjugated to additional components for RMT or
96 other payloads such as imaging contrast agents. Also, it is expensive to engineer and synthesize
97 monoclonal antibodies, which are typically produced in mammalian cell culture. Thus, there is an unmet
98 need for smaller, less expensive, and easier to engineer system for BBB transcytosis.
99
100 Camelids produce functional antibodies devoid of light chains called heavy chain-only antibodies
101 (HCAbs) [21, 22]. HCAbs recognize their cognate antigens by one single domain, the variable domain
102 (VHH). The VHH in isolation is very small compared with other antibodies. The molecular weights of
103 VHHs are typically ~15kDa, which is about 1/10 of the molecular weight of a conventional IgG and about
104 half the molecular weight of a single chain variable fragment (Scfv) [22, 23]. VHHs have affinities at the
105 same order of magnitude as conventional IgGs, often in the nanomolar or subnanomolar range [24].
106 Because of their small size, VHHs can also bind to epitopes not recognized by conventional antibodies
107 and can have better tissue penetration capacities [25, 26]. Caplacizumab was the first VHH approved by
108 FDA for treatment of acquired thrombotic thrombocytopenic purpura in humans [27]. There are several
109 more VHHs which are in clinical trials, with safety profiles similar to other antibody therapeutics in
110 humans [28, 29]. Importantly, VHHs have been found that can facilitate BBB penetration and allow
111 brain target binding. The use of VHHs for BBB transcytosis and target engagement is promising.
112 Specifically, Stanimirovic et al. identified an insulin-like growth factor 1 receptor binding VHH which
113 crosses the BBB by receptor mediated transcytosis [30, 31]. Danis et al. identified and optimized VHHs to
114 mitigate brain accumulation of pathological tau in a tauopathy mouse model [32]. Dupre et al.,
115 identified VHHs which could be used to detect tau in transgenic mice brain tissues [33]. However, the
116 extent to which VHHs that engage in receptor mediated transcytosis using the TfR can carry diagnostic

117 and therapeutic payloads across the BBB still has not been assessed. Here we tested the hypothesis that
118 VHHs that bind to TfR and cross the BBB through RMT in mice could be coupled with additional VHHs
119 that bind to amyloid plaques as a proof of concept for a platform which could be generalized to other
120 neurological diseases.
121
122 Current methods to evaluate BBB crossing require substantial resources and can be time-consuming [17,
123 34]. An efficient way to screen for BBB crossing *in vivo* would be helpful since *in vitro* models may not be
124 fully predictive of *in vivo* results. Neurotensin (NT) is a 13 amino acid peptide first identified by Carraway
125 and Leeman in 1973 from bovine hypothalamic extracts [35]. NT is expressed in CNS as well as in
126 peripheral tissues, mostly in the gastrointestinal tract. NT is involved in regulating appetite, nociception,
127 and thermoregulation in the CNS, and alters nutrient absorption, gastrointestinal motility, and secretion
128 in the peripheral gastrointestinal tract [36]. It was found that NT induces rapid and transient
129 hypothermia in mice and rats when injected to CNS [37, 38]. The hypothermia was likely to be due to
130 effects in hypothalamus. Young & Kuhar found that NT receptors had moderate to high densities in
131 hypothalamus [39]. Injection of NT to medial, lateral preoptic area and anterior parts of hypothalamus
132 induced the hypothermia effect [39]. Meanwhile, intravenously injected NT does not typically cause
133 hypothermia [40]. On the other hand, when NT-conjugated mouse TfR (mTfR)-binding VHHs were
134 injected intravenously to mice, the NT-mTfR VHH conjugates induced hypothermia in mice, presumably
135 because they get across the BBB and bind to NT receptors in hypothalamus [34, 41]. These properties of
136 the NT system make it an apparently attractive assay platform for rapid testing of VHH BBB transcytosis.
137

138 Here, we independently generated additional mTfR-binding VHHs and used a similar NT based modular

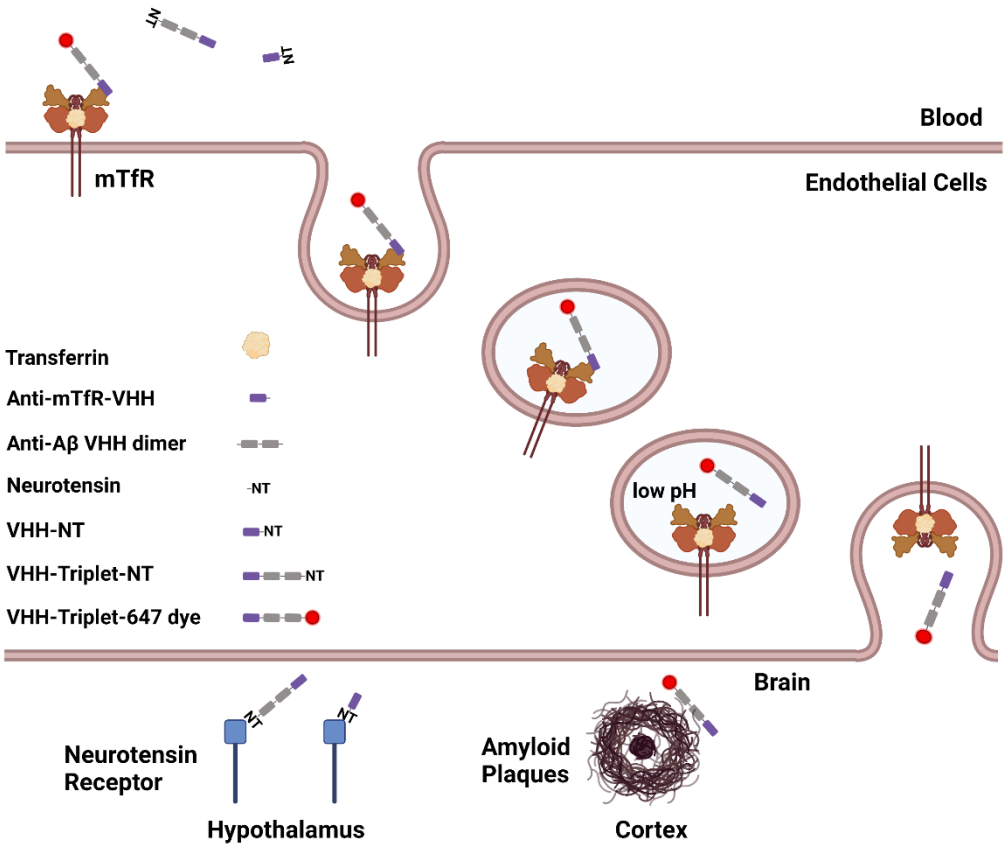

Fig. 1. Schematic of the modular system for VHH-mediated BBB transcytosis and target engagement. Module 1: anti-mTfR VHH for RMT across BBB. Module 2: neurotensin peptide (NT) for rapid assessment of *in vivo* target engagement via measurement of hypothermia. Module 3: anti-Aβ VHH dimer for disease-relevant target engagement in brain parenchyma. Module 4: 647 dye for visualization of VHH constructs in situ. The anti-mTfR VHH was combined with NT for anti-mTfR VHH screening through monitoring hypothermia effect. The anti-mTfR VHH were combined with VHH dimer and NT or 647 to test the effect of anti-mTfR VHH together with other components of the module. This schematic figure also shows the TfR mediated transcytosis across BBB. The anti-mTfR VHH conjugates binds to TfR on the endothelial cells which comprise a major portion of the BBB. Then the TfR-VHH complex is endocytosed across the endothelial cells in the endosomes. VHHs dissociate from the TfR-VHH complex with decreased pH level in endosome and are released on the brain side of the BBB. There were two different targets in the brain parenchyma in this study, the NT receptor in hypothalamus and amyloid plaques in cortex and hippocampus. (Figure generated using BioRender.com)

139 system to screen these VHHs for mTfR-mediated BBB transcytosis (**Fig. 1**). We hypothesized that this

140 modular screening system can be used to identify and optimize anti-mTfR VHHs for BBB transcytosis and

141 brain target binding.

142 This screening system includes four modules. The first module is an anti-mTfR VHH for receptor

143 mediated transcytosis across the BBB; the second module is the neurotensin peptide for assessment of

144 target engagement *in vivo* through measurement of hypothermia. The third module is a dimer of anti -
145 Aβ VHHs for disease-relevant brain target engagement. The fourth module is a fluorescence dye for
146 visualization of VHH constructs in situ. We tested different VHH variants and found one variant which
147 showed good BBB penetration based on this screening system. The VHH variant with the best BBB
148 transcytosis ability fused to a tandem VHH dimer called Nb3-Nb3 which binds to amyloid plaques in
149 brain parenchyma. This VHH triplet was conjugated to a fluorescent dye and post-mortem confocal
150 microscopy was performed to directly evaluate brain target engagement.

151

152 **Methods**

153 **Immunization of llama with mouse transferrin receptor.**

154 A single adult male llama (*Lama glama*) was immunized under contract agreement through Triple J
155 Farms (Kent Laboratories, Bellingham, WA) following the method previously described [42]. Briefly,
156 subcutaneous injections of 100 µg ectodomain (Cys89-Phe763) mTfR (50741-M07H, SinoBiological) were
157 performed with protein emulsified with complete Freund's adjuvant on day 0, followed by additional
158 100 µg immunizations emulsified with incomplete Freund's adjuvant on days 14, 28, and 42. On day 49,
159 peripheral blood was drawn for peripheral blood mononuclear cell (PBMC) isolation. Triple J Farms
160 operates under established National Institutes of Health Office of Laboratory Animal Welfare Assurance
161 certification number A4335-01 and United States Department of Agriculture registration number 91-R-
162 0054.

163 **Generation of VHH immune phage display library.**

164 The generation of an immune phage display library and isolation of mTfR binding VHH clones was
165 performed using the methods previously described [42]. Briefly, total RNA extracted from PBMCs was

166 used for synthesis of first-strand complimentary DNA (cDNA) using the SuperScript IV First-Strand
167 Synthesis kit (#1891050, Invitrogen). The heavy-chain variable domain was then amplified from the
168 cDNA using Q5 high-fidelity DNA polymerase (New England Biolabs) with the described primers
169 (CALL001: 5′ -GTCCTGGCTGCTCTTCTACAAGG-3′ and CALL002: 5′ -GGTACGTGCTGTTGAACTGTTCC-
170 3'). The heavy-chain specific amplicon was isolated using electrophoresis with low-melting point agarose
171 extraction with the QIAquick Gel Extraction kit (Qiagen). A secondary amplification was performed using
172 a modification of the primers (VHH-Esp-For: 5′ -
173 CCGGCCATGGCTGATGTGCAGCTGCAGGAGTCTGGRGGAGG-3′ and VHH-Esp-Rev: 5′ -
174 GTGCGGCCGCTGAGGAGACGGTGACCTGGG T-3′) used by Pardon et al. to facilitate cloning into the
175 phagemid pHEN2 [43]. The amplified sequences were cleaved with the restriction endonucleases NcoI
176 and NotI (New England Biolabs) and subsequently ligated into compatibly cleaved pHEN2 phagemid at a
177 3:1 (insert:phagemid) ratio overnight at 16°C followed by purification. The resulting ligation mixture was
178 electroporated into TG-1 phage-display competent cells (#60502-1, Lucigen) and plated onto 2xYT agar
179 containing 100 µg/mL carbenicillin and 2% (w/v) glucose at 37°C overnight. The resulting library
180 contained > 10^7 independent clones. Phage was produced for screening using the M13KO7 helper phage
181 (#18311019, Invitrogen) followed by precipitation by addition of one-fifth volume 20% polyethylene
182 glycol 6000 / 2.5 M sodium chloride solution on ice and centrifugation to purify the phage particles.
183
184 **Immunopanning and clone screening.**
185
186 Selection of mTfR specific VHH was performed using direct binding of phage to immobilize mTfR.
187 Standard radioimmunoassay (RIA) tubes were coated with 500 µL mTfR solution at 5 µg/mL in sodium
188 carbonate buffer, pH 9.6 overnight at 4°C. The coating solution was removed, and the RIA tube filled

189 with a 2% (w/v) non-specific blocking solution (bovine serum albumin or nonfat dry milk) in 1x
190 Phosphate Buffered Saline (PBS). Amplified phage (~10^{11} phage) was mixed with blocking solution to a
191 final volume of 500 µL and then transferred into the RIA tube to allow for association at room
192 temperature and 600 rpm mixing. The RIA tube was then washed 20 times with 1x PBS and then the
193 bound phage eluted with 100 mM triethylamine solution for 20 mins. The eluted phage solution was
194 neutralized with 1:10 volume 1 M Tris-HCl, pH 8.0. The eluted phage was amplified in TG-1 cells and a
195 second round of immunopanning was performed.
196
197 Following the second round of immunopanning, individual colonies were selected and cultured in 96-
198 well blocks containing 2xYT containing carbenicillin at 37°C with 300 rpm shaking for 4-6 hours.
199 Expression of VHH was induced by addition of isopropyl-beta-D-thiogalactoside (IPTG) to a final
200 concentration of 1 mM and incubation overnight at 37°C. The culture blocks were centrifuged to pellet
201 the cells and frozen at -80°C for 1 hour following removal of the culture supernatant. The culture block
202 was then equilibrated to room temperature and 500 µL 1xPBS added to each well followed by shaking at
203 1500 rpm to resuspend the cell pellets and allow for release of VHH from the cells. The culture block was
204 centrifuged for 20 min at 2000xg. Nunc Maxisorp plates were coated with mTfR at 1 µg/mL as described
205 above and blocked with 1% bovine serum albumin (BSA). The clarified VHH supernatants were incubated
206 on the mTfR plates for 1 hour at room temperature. The assay plate was washed and peroxidase
207 conjugated goat anti-alpaca VHH domain specific antibody (#128-035-232, Jackson ImmunoResearch) at
208 0.8 µg/mL was transferred to the plate and incubated for 1 hour at room temperature. Following a final
209 wash, the assay was developed by addition of tetramethylbenzidine (#T5569, Sigma-Aldrich) and
210 absorbance was measured at 650 nm on a Biotek Synergy 2 plate reader. Clones with absorbance values
211 greater than two standard deviations above background were considered of interest and subsequently
212 sequenced.

213

214 **Amyloid beta specific VHH production.**

215 Paraschiv et al. previously reported the isolation of amyloid beta binding VHH clones [44]. We selected
216 the sequence for the named Nb3 clone for use in this study. The Nb3 amino acid sequence was imported
217 into SnapGene software (GSL Biotech LLC) and reverse translation performed using preferred codon
218 usage for expression in *E. coli*. Additional sequence, including a $(Gly\text{-}Gly\text{-}Gly\text{-}Ser)_3$ between VHH
219 domains, was incorporated for cloning into pHEN2 as a tandem dimer as part of the heterotrimer clones
220 synthesized with TfR binders. To reduce the potential for recombination events, the DNA sequence was
221 manually curated to adjust the codon usage and reduce the frequency of repetitive sequence within the
222 Nb3-Nb3 dimer. The affinity of the Nb3-Nb3 dimer was measured using bio-layer intergerometry as
223 described below.

224 **Bio-layer interferometry (BLI) assessment of VHH binding kinetics.**

225 The binding kinetics of the selected VHH clone against mTfR and Aβ was assessed by BLI. For
226 measurements of mTfR kinetics, biotinylated VHH was diluted into assay buffer at 1 µg/mL and
227 immobilized onto streptavidin coated biosensors (#18-5019, Sartorius) to a minimum response value of
228 1 nm on the Octet Red96 System (Sartorius). For measurements of amyloid beta, beta-amyloid(1-40)-
229 Lys(biotin-LC) (AS-23517, Anaspec), was diluted into assay buffer at 1 µg/mL and immobilized onto
230 streptavidin coated biosensors (#18-5019, Sartorius) to a minimum response value of 1 nm on the Octet
231 Red96 System (Sartorius). Purified mTfR or VHH clones were diluted into assay buffer at the specified
232 concentrations. The immobilized antigen biosensors were allowed to associate at 37C° followed by
233 dissociation in the baseline buffer well location. All assays included a background correction condition to
234 allow for sensor normalization. The ForteBio Data Analysis suite was used to normalize the association
235 curves following background subtraction and Savitzky-Golay filtering. Curve fitting was applied using

236 global fitting of the sensor data and a steady state analysis calculated to determine the association and
237 dissociation constants. All assay steps were prepared in Greiner 96-well plates (#655209) in a volume of
238 300 µL. Assay buffer was defined as 0.1% BSA (w/v) in 1xPBS.

239 **Synthesis and expression of VHH constructs.**

240 Based on the methods described in **Immunopanning and clone screening** and **BLI assessment of VHH**
241 **binding kinetics** sections, we synthesized several neurotensin-fused VHH monomers with different
242 binding affinities to mouse transferrin receptor. In addition, we produced single polypeptide VHH
243 heterotrimers that consisted of $M1_{P96H}$, a $(Gly\text{-}Gly\text{-}Gly\text{-}Ser)_3$ linker, Nb3, a $(Gly\text{-}Gly\text{-}Gly\text{-}Ser)_3$ linker, and
244 Nb3 using the method described in **Amyloid beta specific VHH production**. The VHH dimer Nb3-Nb3
245 binds to amyloid plaques in brain parenchymal of APP/PS1 mice. These constructs were termed "$M1_{WT}$-
246 NT", "$M1_{P96H}$-NT", "$M1_{AA}$-NT", "$M1_{R100dH}$-NT" and "$M1_{P96H}$-triplet". The VHH naming convention for P96H
247 and R100dH are based on the Kabat nomenclature and refer to the specific amino acid residue
248 modification positions within the VHH sequence [45]. Another neurotensin fusion with a VHH generated
249 against human TfR, which does not bind mouse TfR called "H1-NT," was used as control. All VHH
250 constructs were designed using SnapGene Software and synthesized (Twist Bioscience) with
251 corresponding restriction endonuclease sites for direct cloning into pHEN2. Sequence confirmed pHEN2
252 clones with the various constructs were transferred into BL21(DE3) competent *E. coli* cells (C2527I, New
253 England Biolabs). Transformed cells were grown in terrific broth medium containing carbenicillin at 37°C
254 and 300rpm shaking in baffled flasks. Once the culture density reached an optical density equal to 0.6,
255 IPTG was added to a final concentration of 1mM to induce protein expression. For monomer VHH
256 expression the post-induction incubation temperature was maintained at 37C but reduced to 30C for
257 the $M1_{P96H}$-triplet. Following overnight expression, cells were pelleted by centrifugation and VHHs were
258 extracted through osmotic shock and recovery of the periplasmic fraction [42, 46]. Clarified periplasmic
259 fraction was purified using HisPur™ Ni-NTA Resin (88222, Thermo Fisher Scientific) column

260 chromatography. The eluted VHH proteins were further purified by size-exclusion chromatography (SEC)
261 over a Superdex75 10/300 column on an AKTA Pure (Cytiva). Protein purity was assessed by SDS-PAGE
262 on a 10% Bis-Tris MES acrylamide gel and found to be >95% pure.

263 $M1_{P96H}$-triplets and H1-triplets were fluorescently labeled with using Alexa Fluor™ 647 succinimidyl ester
264 dye to allow fluorescence confocal microscopy of tissue sections. The triplets were incubated with the
265 succinimidyl ester dye for 1 hour in 50mM sodium carbonate buffer, pH 9.6 and purified by desalting
266 using a 5mL HiTrap desalting column in-line with the AKTA Pure. The binding fidelity of the VHH
267 heterotriplet was assessed by ELISA against mTfR. The fluorescence dye labeled $M1_{P96H}$-triplet and H1-
268 triplet were named "$M1_{P96H}$-triplet-647" and "H1-triplet-647"

269 **Endotoxin removal**.

270 Removal of contaminating endotoxin was achieved using High-Capacity Endotoxin Removal Resin
271 (88270, Pierce) from the VHH preparations. A volume of 0.25ml endotoxin removal resin was added to
272 1ml of VHH sample. The VHH and resin were mixed for 2hr at room temperature to allow for absorption
273 of endotoxin. The mixture was centrifuged to pellet the resin and the supernatant collected. A volume of
274 0.25ml fresh endotoxin removal resin was added to the first-pass solution and mixed for another 2hr at
275 room temperature. Following a final centrifugation to pellet the resin, the solution was collected for
276 endotoxin level testing. Endotoxin levels were measured using the Chromagenic Endotoxin Quant kit
277 (A39552, Pierce) according to the manufacturers protocol to ensure a level of endotoxin <0.5 endotoxin
278 units/mg of total protein.

279 **Binding assessment of histidine mutations by ELISA**.

280 To determine the effect on histidine mutation introduction, an ELISA was performed with the post VHH
281 binding wash buffer at normal and reduced pH. Nunc Maxisorp plates were coated with mTfR at 1
282 µg/mL in 50mM sodium carbonate, pH 9.6 overnight at 4°C. The plates were blocked with 1% BSA in

283 1xPBS buffer and then triplicate dilutions of each VHH prepared in 0.5% BSA in 1xPBS buffer and
284 transferred to the plate. Binding at room temperature for 2 hours was followed by three cycles of 5-
285 minute washes with either 1xPBS, pH 7.2 or 1xPBS, pH 5.5. Following the pH dependent wash step, the
286 bound VHH was detected with peroxidase conjugated goat anti-alpaca VHH domain specific antibody
287 (#128-035-232, Jackson ImmunoResearch) at 0.8 µg/mL incubated for 1 hour at room temperature.
288 Following a final wash, the assay was developed by addition of tetramethylbenzidine (#T5569, Sigma-
289 Aldrich), the reaction was terminated by addition of 50 µL 1M hydrochloric acid and absorbance was
290 measured at 450 nm on a Biotek Synergy 2 plate reader.

291 **Animals**

292 All animal experiments were conducted under protocols approved by the National Institute of
293 Neurological Disorders and Stroke (NINDS)/ National Institute on Deafness and Other Communication
294 Disorders (NIDCD) Animal Care and Use Committee in the National Institutes of Health (NIH) Clinical
295 Center. C57BL/6J female mice were purchased from Jackson labs at 6-7 weeks of age and used at 7-12
296 weeks of age. Fifteen mice were divided into five groups with three mice in each group to test the five
297 VHH-NT fusions. Anesthetized mice were injected via tail vein with VHH-NT fusions: $M1_{WT}$-NT, $M1_{P96H}$-
298 NT, $M1_{AA}$-NT, $M1_{R100dH}$-NT and H1-NT for screening. Experiments were performed at the same time each
299 day. Three mice were injected with VHH triplet-NT to assess the ability of VHH triplet-NT to get across
300 the BBB. To confirm the result from the five VHH-NT fusions, a blinded replication experiment was
301 performed with additional fifteen mice randomized using a random number generator into five groups
302 with three mice in each group.

303 APP_{SWE}/PSEN1dE9 (MMRRC Strain #034832) positive transgenic mice were purchased from Jackson labs
304 [47, 48], maintained on a hybrid (C57BL/6xC3H) background, and raised under protocols approved by
305 the National Institute of Neurological Disorders and Stroke (NINDS)/ National Institute on Deafness and

306 Other Communication Disorders (NIDCD) Animal Care and Use Committee in the National Institutes of
307 Health (NIH) Clinical Center. Ten transgenic mice ages between 13-15 months, eight males and two
308 females, were randomly assigned to two groups. Five mice were injected with $M1_{P96H}$-triplet-647 and
309 five mice were injected with H1-triplet-647.

310 **Injection of VHH-NTs and VHH-triplet-647s**

311 Mice were anesthetized with 60% oxygen/ 40% medical air gas mixture containing 5% isoflurane in an
312 induction box. After a stable anesthesia plane was established, mice were maintained at 1.5-2%
313 isoflurane level. Artificial tears ointment was applied to prevent eye injury due to drying. Mice were
314 placed on an electrical heating pad to maintain body temperature at 37C°. The VHH-NTs, $M1_{WT}$-NT,
315 $M1_{P96H}$-NT, $M1_{AA}$-NT, $M1_{R100dH}$-NT and H1-NT were injected into wild-type C57BL/6J mice through the tail
316 vein using a 30 Gauge needle in a single bolus at a dose of 600nmol/kg body weight in 1xPBS. The VHH-
317 triplet-647s, $M1_{P96H}$-triplet-647 and H1-triplet-647, were injected intravenously through single bolus
318 injection at a dose of 1000nmol/kg body weight. Mice were maintained under anesthesia for
319 approximately 2-3 minutes. Following the procedure, the mice were allowed to recover on a heating pad
320 until fully ambulatory and then returned to their home cage with immediate access to food and water.

321 **Temperature measurement**

322 Infrared thermometry was used for temperature measurement using an infrared thermometer (Model#
323 62 MAX+, Fluke). Abdominal fur was removed by application of topical depilatory cream prior to
324 temperature measurement for precise data collection. Baseline temperature was measured three times
325 before intravenous (IV) injection with a time interval of 30min between measurements. Then, mouse
326 temperatures were measured at the time intervals of 30min, 1hr, 1.5hr, 2hr, 2.5hr, 3hr, 3.5hr, 4hr, 4.5hr
327 and 5hr after injection. All temperature measurements were performed by investigators blinded to the
328 identity of the injected VHH sample. Mice were briefly anesthetized (<20 seconds) with isoflurane for

329 each temperature measurement. In preliminary experiments we confirmed that this brief anesthesia did
330 not affect temperature.

331 **Confocal microscopy of mice brains injected with triplet-647**

332 Two hours post IV injection mice were sacrificed under isoflurane anesthesia by cardiac perfusion with
333 1X PBS + Heparin (10 units Heparin per milliliter 1X PBS). Following perfusion, mice were decapitated
334 using a pair of sharp surgical shears and the brain was carefully excised from the cranium. Brains were
335 fixed in 4% PFA for 24hrs then equilibrated in 30% sucrose for 48 hours. Then, mouse brains were
336 sectioned at 50 µm thickness using a freezing sliding microtome. Staining was performed to visualize
337 amyloid plaques using the Congo Red derivative X34.[49] Tissue was rinsed with 1xPBS two times. Then,
338 tissues were incubated in 40%EtOH/60%PBS at pH10 containing 10 µM X34 (SML1954-5MG, Sigma) for
339 10min. After X34 incubation, tissue was rinsed with milliQ water five times then differentiated in
340 40%EtOH/60%PBS at pH10 for 2min. After differentiation, the tissue was rinsed with miliQ water for
341 10min then mounted onto positively charged slides (EF15978Z, Daigger®). The mounted tissue sections
342 were allowed to dry overnight at room temperature and cover slipped using fluoromount-G (00-4958-
343 02, Invitrogen™).

344 To objectively evaluate the effect of intravenous injection of $M1_{P96H}$-Triplet-647 and H1-Triplet-647 on
345 APP/PS1 mice, brain sections at around 2.5mm posterior to bregma were selected for confocal
346 fluorescence imaging. The brain sections were equally divided into 10 parts in both horizontal (x) and
347 vertical (y) directions (**Additional file 1: Fig. S1**). X and y coordinates were randomly selected using by
348 random numbers from 1 to 10. When (x, y) coordinates fell onto a cortical area, stacks of images were
349 taken which covered 16µm depth (z direction) starting from the top of the brain section. When (x, y)
350 coordinates fell outside of the cortex, the microscope was moved to the next randomized (x, y)
351 coordinates without taking images. Brain sections were imaged using a Zeiss LSM 510 microscope.

352 Stacks of images were acquired with eight images per stack and 2µm optical thickness at 20x
353 magnification using a Zeiss Plan-Apochromat 20x/0.8NA lens. Images were acquired using laser
354 wavelength at 633nm to visualize the VHH triplets conjugated with 647 dye and 405 nm wavelength
355 laser to visualize the X-34 dye. For 647 channel images, laser at wavelength 633nm was used with a
356 LP650 filter and laser power set to be at transmission 100%. For X34 channel images, laser at
357 wavelength 405nm was used with a BP420-480 filter and laser power set to be at transmission 15%. The
358 images were exported in lsm file format for image analysis using ImageJ.

359 **Fluorescent confocal microscopy - Naïve brain as controls**

360 Naïve APP/PS1 positive mouse brain sections stained only with X-34 for fluorescence confocal
361 microscopy were used as a negative control. Naïve APP/PS1 positive mouse brain sections stained with
362 both X34 and *ex vivo* $M1_{P96H}$-Triplet-647 for fluorescence confocal microscopy were used as a positive
363 control. For *ex vivo* $M1_{P96H}$-Triplet-647 staining, naïve brains were sectioned and washed in 1XPBS.
364 Sections were incubated in 3% normal donkey serum for 30min to block non-specific binding. After
365 blocking, tissue sections were incubated overnight at 4C° in $M1_{P96H}$-Triplet-647 at a concentration of
366 10ug/ml in blocking solution. Tissues were then washed in 1xPBS three times followed by X34 staining as
367 described.

368 **Automated image analysis**

369 To quantitatively analyze the confocal microscope images, thresholding and particle analysis were
370 performed to remove background signals and isolate target structures of interest. The percent area of
371 X34 stained amyloid plaques was quantified with thresholding at (0, 30) followed by Particle analysis. To
372 remove low signal background, 647 channel image thresholding was set at 0-1000. Then the 647 channel
373 images was analyzed with particle analysis. The parameters for particle analysis were set to be 0-1000
374 pixels for size and 0.1-1.0 for circularity. The parameters for thresholding and particle analysis were

375 determined through testing of different parameters to capture the qualitative morphology of amyloid
376 plaques as assessed by experienced investigators. Amyloid plaque levels were represented as % area of
377 X34 coverage and VHH triplet-647 entry into the brain parenchyma was represented as % area of Alexa
378 647 dye coverage in the areas with X34 staining. Because there is mouse-to-mouse variability in plaque
379 size and X34 staining intensity, we analyzed the ratio of the Triplet-647 coverage to X34 coverage.

380 **Statistical analysis**

381 Unpaired student t-test were performed to evaluate the differences between the transcytosis ability of
382 $M1_{P96H}$-triplet-647 and H1-triplet-647 to amyloid plaques in APP/PS1 transgenic mice brains. Graphs
383 were created using Prism. Sample sizes were based on availability of transgenic mice and previous
384 experiments. No formal power calculations were performed.

385

386 **Results**

387 **Endotoxin removal**

388 VHHs contamination by endotoxins is a byproduct of expression in *E. Coli* cells [50]. Endotoxin can
389 induce systemic inflammation and cause disruptive BBB changes [51]. It was found that the excess
390 endotoxin level in VHH-NT fusions can cause additional hypothermia (**Additional file 1: Fig. S2**). To avoid
391 potential hypothermia effects caused by endotoxin, endotoxin was removed after purification. After
392 endotoxin removal, the level of endotoxin level in VHHs was less than 0.1 endotoxin unit/ml (EU/ml)
393 within normal range [52].

394 **Anti-mTfR VHH variant screening based on binding affinity measurement**

395 VHH monomer-NT (M1-NT and H1-NT) and VHH-heterotrimer-NT ($M1_{P96H}$-triplet-NT) had characteristics
396 consistent with expectation. **Fig. S3 and S4** showed the SDS-PAGE gel and exemplar size-exclusion

397 column results of the VHH monomer-NT and VHH-heterotrimer-NT after purification (**Additional file 1:**
398 **Fig. S3 and S4**). VHH monomer-NTs had size around 14kDa (**Additional file 1: Fig. S3**) and VHH
399 heterotrimer-NTs had size between 38-49kDa (**Additional file 1: Fig. S4**).

400 Histidine mutations could potentially impart pH dependence of binding [53]. Histidine protonation at
401 lower pH-values can increase dissociation rate of antibodies to their receptors. Maeda et al. found that
402 the dissociation rate was less rapid in the intracellular acidic compartments once histidine was deleted
403 from human epidermal growth factor [54]. In this study, we generated different M1 variants based on
404 the effect of histidine on VHH dissociation rate. **Fig. S5.** shows the mTfR ELISA on M1 variants: $M1_{P96H}$,
405 $M1_{WT}$ and $M1_{R100dH}$ (**Additional file 1: Fig. S5**). Comparing M1 variant binding to mTfR under normal
406 physiological pH (pH = 7.2) and acidic pH (pH = 5.5), lower pH did not alter the dissociation of $M1_{WT}$ to
407 mTfR but substantially impacted the dissociation of $M1_{P96H}$ to mTfR.

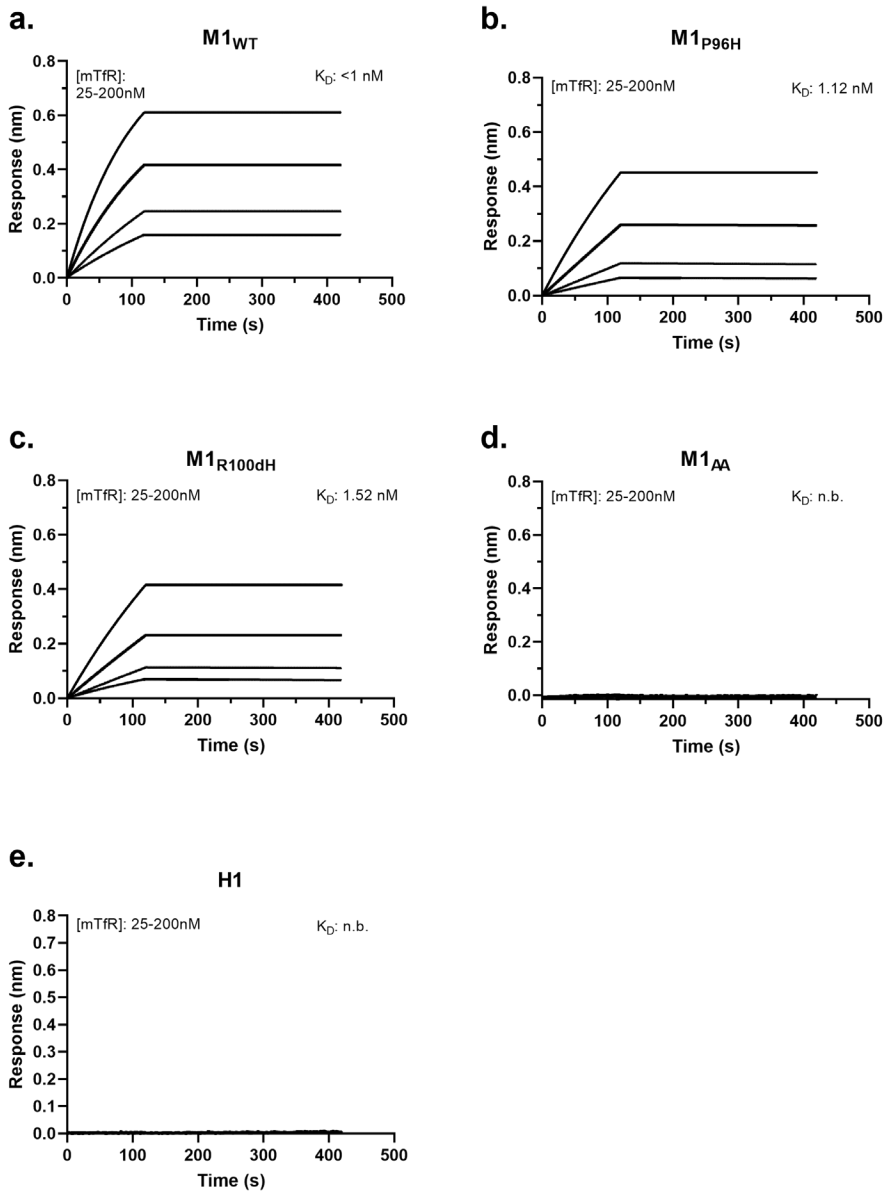

Fig. 2. Affinity binding curves of the five M1-NT variants: $M1_{WT}$-NT (**a.**), $M1_{P96H}$-NT (**b.**), $M1_{R100dH}$-NT (**c.**), $M1_{AA}$-NT (**d.**) and H1-NT (**e.**) binding affinity (K_D) to mTfR. Using biolayer interferometry on an Octet Red96 system, association and dissociation rates were determined by immobilizing biotinylated VHH onto streptavidin-coated optical sensors. The M1-NT variant association and dissociation curves to mTfR were plotted and the affinity of each to mTfR was calculated. (n.b. = no binding)

408 Then the affinity of M1 variants to mTfR was measured using Octet. Based on Octet measurement, the

409 affinity (KD) of $M1_{WT}$-NT, $M1_{P96H}$-NT, and $M1_{R100dH}$-NT to mTfR were <1nM, 1.12nM, 1.52nM. While the

410 affinity (KD) of $M1_{AA}$-NT and H1-NT to mTfR was not detectable. **Fig. 2** shows the association and

411 dissociation curves of the $M1_{WT}$-NT, $M1_{P96H}$-NT, $M1_{AA}$-NT, $M1_{R100dH}$-NT and H1-NT to mTfR. $M1_{WT}$-NT,

412 $M1_{P96H}$-NT, and $M1_{R100dH}$-NT bond to mTfR well while $M1_{AA}$-NT and H1-NT showed no binding.

413

414 **M1 variant screening for BBB transcytosis using neurotensin fusion and hypothermia assessment**

415 To assess BBB transcytosis ability, several M1 variants were fused to NT and screened based on the

416 extent of hypothermia effects. Three M1 variant NT fusions, including $M1_{WT}$-NT, $M1_{R100dH}$-NT and $M1_{P96H}$-

417 NT were injected to WT mice. NT alone was injected into WT mice at the same molarity as an initial

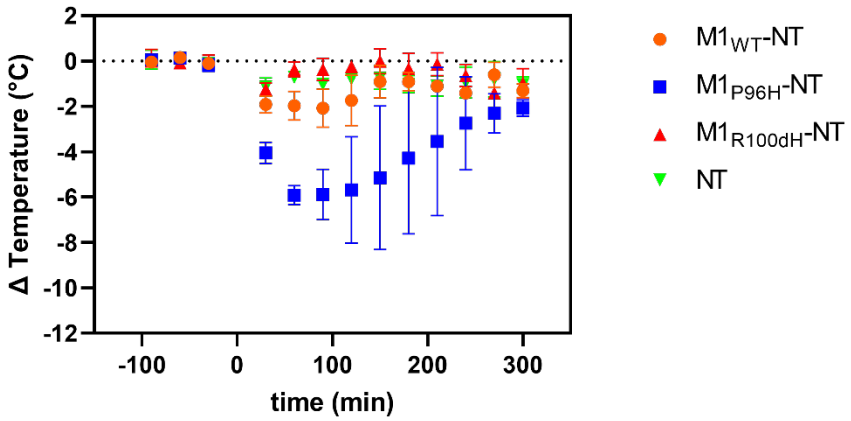

Fig. 3. The use of NT fusion to VHHs for VHH screening via hypothermia as an indication of CNS target engagement. The M1 variants with different affinities to mTfR have different hypothermic effects. Among the three M1 variants injected to mice at the same dose 600nmol/kg body weight (n = 3 per group), $M1_{P96H}$-NT produced the most prominent hypothermia effect, with a maximum temperature drop of about 6C° and duration for about 4hrs.

418 negative control. At a dose of 600nmol/kg body weight, the M1 variants with different binding affinities

419 to mTfR show different hypothermia effects (**Fig. 3**). $M1_{WT}$-NT reduced temperatures by approximately

420 2C°, with an effect that lasted approximately 2 hours. $M1_{P96H}$-NT, at the same dose, decreased

421 temperature by 6C° with effects that lasted more than 4 hours, indicating that $M1_{P96H}$-NT appeared to

422 improve CNS penetration. NT alone did not show any hypothermia effect, indicating that peripherally

423 administered NT alone does not appear to cross the BBB into the CNS. $M1_{R100dH}$-NT gave less than 2C° of

424 hypothermia effect. Mouse body temperatures were stable at baseline.

425 To confirm and extend these findings, a blinded experiment was performed. The previous three M1

426 variants, plus a fourth mutant $M1_{AA}$-NT that has minimal TfR binding and a different VHH that binds to

427 human TfR called H1 were tested by an investigator blinded to the identity of the injected materials.

428 $M1_{AA}$-NT and H1-NT were tested at a higher molarity in a previous experiment and showed no obvious

429 hypothermia effects (**Additional file 1: Fig. S6**). The blinded experiment results were consistent with the

430 previous finding: $M1_{P96H}$-NT clearly reduced the temperature the most, with a maximum drop of about

431 4C°. The other M1-NTs and H1-NT did not reduce the temperature substantially (**Fig. 4**). These results

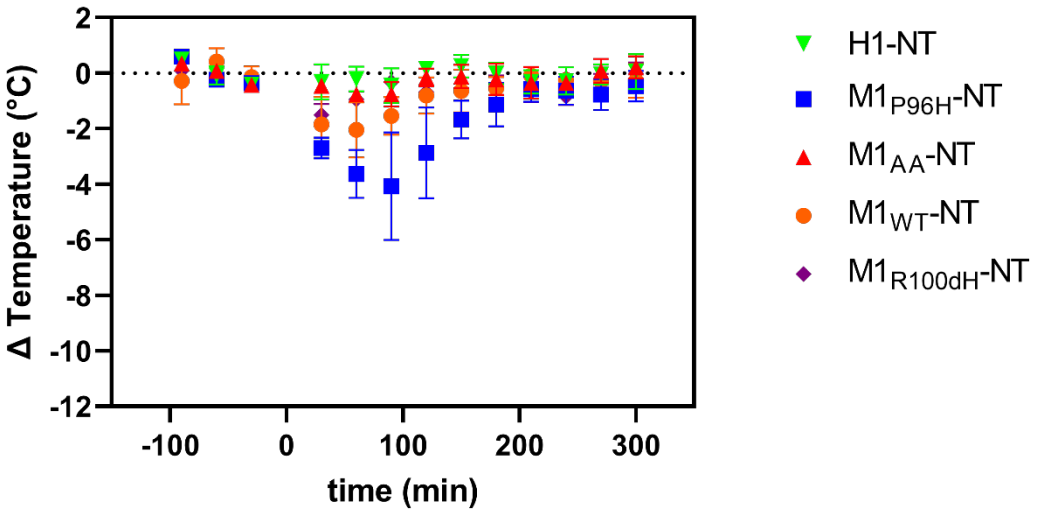

Fig. 4. Hypothermic effect of M1 VHH-NT fusions in a randomized, blinded cohort. Five VHH-NT fusions $M1_{WT}$-NT, $M1_{P96H}$-NT, $M1_{AA}$-NT, $M1_{R100dH}$-NT and H1-NT were blinded by an independent investigator. Each blinded VHH-NT fusion was injected in a randomized fashion at a dose of 600nmol/kg body weight (n=3 per group) and body temperature measured over the indicated time interval. Following complete data collection of the temperature measurements, the results were unblinded. Consistent with previous finding, $M1_{P96H}$-NT gave the most prominent hypothermia effect.

432 indicate that temperature measurement experiments facilitated the identification of an anti-mTfR VHH

433 variant which induced substantial CNS effects.

434 **$M1_{P96H}$-NT dose effect**

435 To understand whether the amount of $M1_{P96H}$-NT injected to mice affects the extent of hypothermia

436 effects, we injected $M1_{P96H}$-NT to WT mice at four different doses: 67nmol/kg body weight, 200nmol/kg

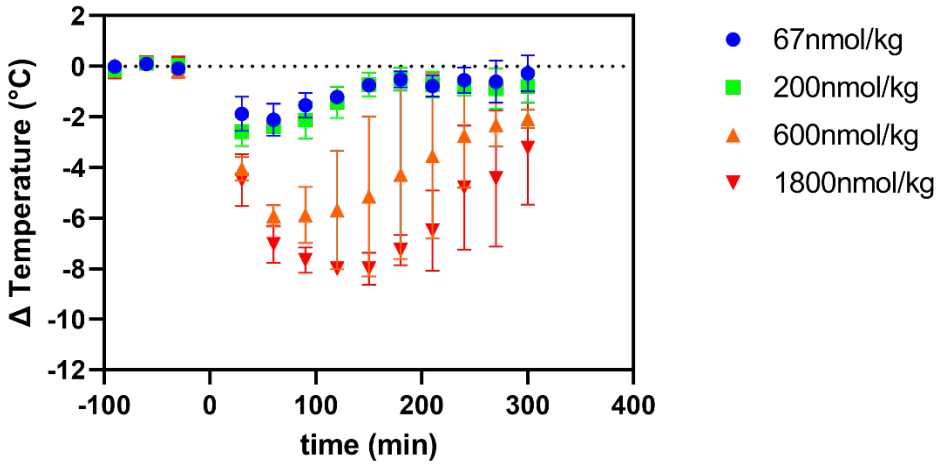

Fig. 5. $M1_{P96H}$-NT dose effect in WT mice after IV injection. This figure shows the dose effect of $M1_{P96H}$-NT in WT mice after tail vein injection (n = 3 per group). The hypothermia effect was stronger and lasted longer time with dose increased from 67nmol/kg body weight to 1800nmol/kg body weight.

437 body weight, 600nmol/kg body weight, and 1800nmol/kg body weight. Twelve mice were used in this

438 experiment, with three mice at each dose (**Fig. 5**). At the two lower doses, there was minimal

439 hypothermia effects. With increased $M1_{P96H}$-NT concentration, the maximum temperature drop

440 increased to about 8C° and also the duration of hypothermia was extended to as long as 5 hours. Thus,

441 these was an apparently monotonic dose-response relationship between intravenous $M1_{P96H}$-NT and

442 hypothermia.

443 **Temperature effect of $M1_{P96H}$-Triplet-NT**

444 Based on the octet results and temperature measurement, $M1_{P96H}$ was chosen as the variant to use to

445 assess ability to cross the BBB after conjugating to a payload. As a proof of concept, we used the anti-Aβ

446 VHH dimer Nb3-Nb3 as the payload fused in a single polypeptide with $M1_{P96H}$ and NT and named $M1_{P96H}$-

447 Triplet-NT, the $M1_{P96H}$-Triplet NT, was injected intravenously into three WT mice. Body temperature was

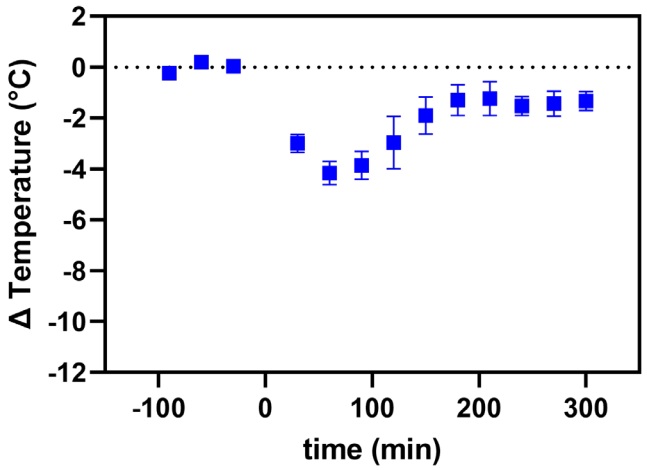

Fig. 6. Measurement of $M1_{P96H}$-Triplet-NT hypothermia effect. $M1_{P96H}$-Triplet-NT was injected at dose of 600nmol/kg body weight (n = 3) and caused a temperature drop of about 4C°.

448 measured as described in the Temperature measurement section. **Fig. 6** shows the temperature change

449 after tail vein injection of $M1_{P96H}$-Triplet-NT. There was about 4C° temperature drop after the

450 intravenous injection and the hypothermia effect peaked at about 1 hour post injection. This result

451 confirmed that after fusing to an anti-Aβ VHH dimer payload, the $M1_{P96H}$-Triplet-NT was still able to get

452 across the BBB and exert a CNS effect.

453 **Affinity measurement of VHH-Triplet**

454 To confirm that fusion with Nb3-Nb3 did not affect the binding ability of $M1_{P96H}$ and Nb3-Nb3 dimer to

455 their targets, the affinity of $M1_{P96H}$-triplet to mTfR and to Aβ were measured to be 1.63nM and 9.98nM

456 using Octet (**Additional file 1: Fig. S7**). The affinity of the $M1_{P96H}$-triplet to mTfR was on the same order

457 before and after the fusion. The affinity of H1-Triplet-647 to mTfR and Aβ was also assessed using Octet

458 and measured to be no binding to mTfR and 9.44nM to Aβ (**Additional file 1: Fig. S7**). It was verified that

459 the fusion of $M1_{P96H}$ and H1 to VHH dimer Nb3-Nb3 did not change their binding affinities.

460 To ensure that the dye labeling did not affect $M1_{P96H}$-triplet binding to mTfR, a mTfR ELISA on $M1_{P96H}$-

461 triplet before and after Alexa 647 dye labelling was performed. The binding curves before and after

462 labeling overlapped with each other (**Additional file 1: Fig. S8**), indicating that the Alexa 647 dye labeling

463 did not affect the binding.

464 **Direct assessment of brain target engagement after intravenous injection of VHHs using confocal**

465 **microscopy**

466 VHH-Triplets were injected to APP/PS1 positive transgenic mice to directly assess brain target (Aβ)

467 engagement. Ten transgenic mice were randomized into two groups, with five mice in each group. Five

468 mice were injected with $M1_{P96H}$-Triplet-647 and five mice were injected with H1-Triplet-647 as a

469 negative control which does not bind to mTfR. Because the hypothermia effect was most prominent in

470 the first two hours post injection in previous experiments using NT fusions, transgenic mice were

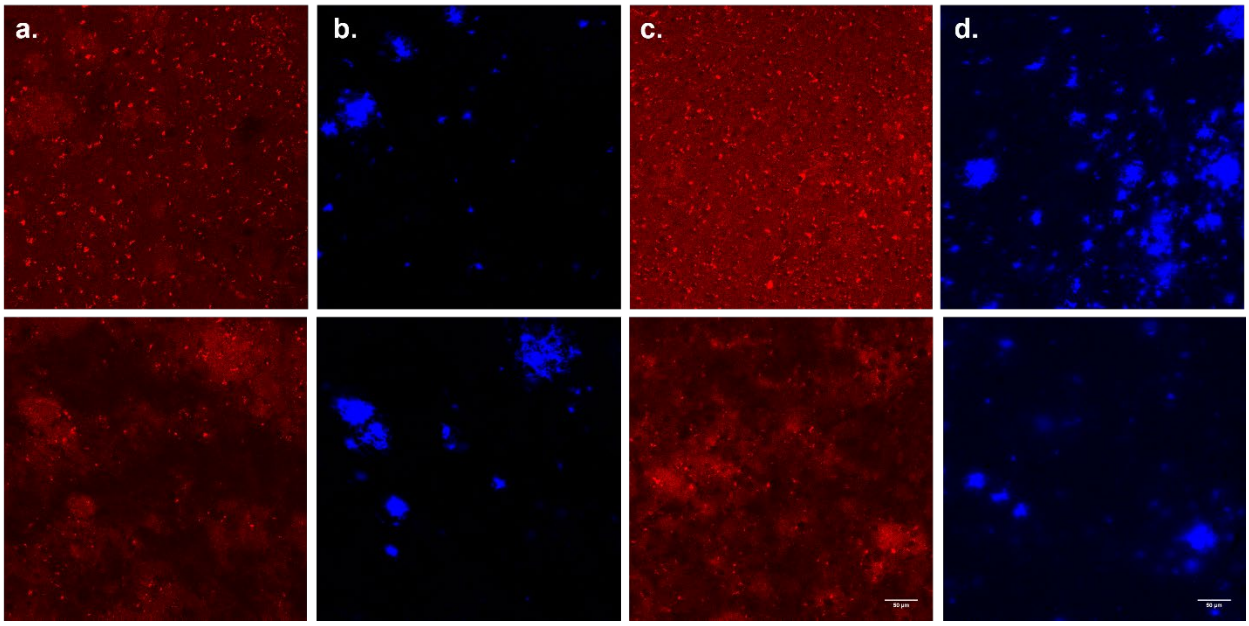

Fig 7. Representative immunofluorescent confocal microscopy of mice brains 2 hours after intravenous injection. 647 channel (**a.**) and X34 channel (**b.**) microscopy of mice brains injected with H1-Triplet-647. 647 channel (**c.**) and X34 channel (**d.**) microscopy of mice injected with $M1_{P96H}$-Triplet-647.

471 sacrificed two hours post IV injection. **Fig. 7** shows exemplar confocal images of brains injected with

472 $M1_{P96H}$-triplet-647 or H1-triplet-647. From the exemplar images, it appeared that most of the 647 signals

473 were similar to background, with some areas that had morphology consistent with amyloid plaque

474 labeling. However, surprisingly, the confocal imaging patterns were similar in both $M1_{P96H}$-triplet-647

475 and H1-triplet-647 injected mice, suggesting a modest amount of non-specific BBB crossing and Aβ

476 plaque binding plus background autofluorescence, rather than the expected extensive mTfR-mediated

477 transcytosis and Aβ plaque binding.

478 To confirm that the lack of anti-Aβ plaque binding after IV injection by $M1_{P96H}$-triplet-647 was not caused

479 by the inability of the Nb3-Nb3 to label Aβ in the context of the $M1_{P96H}$-triplet-647 fusion construct, an

480 *ex vivo* labeling experiment was performed. We labeled brain sections from a naïve APP/PS1 positive

481 mouse with $M1_{P96H}$-Triplet-647 using modest concentrations and no antigen retrieval. **Fig. 8** shows that

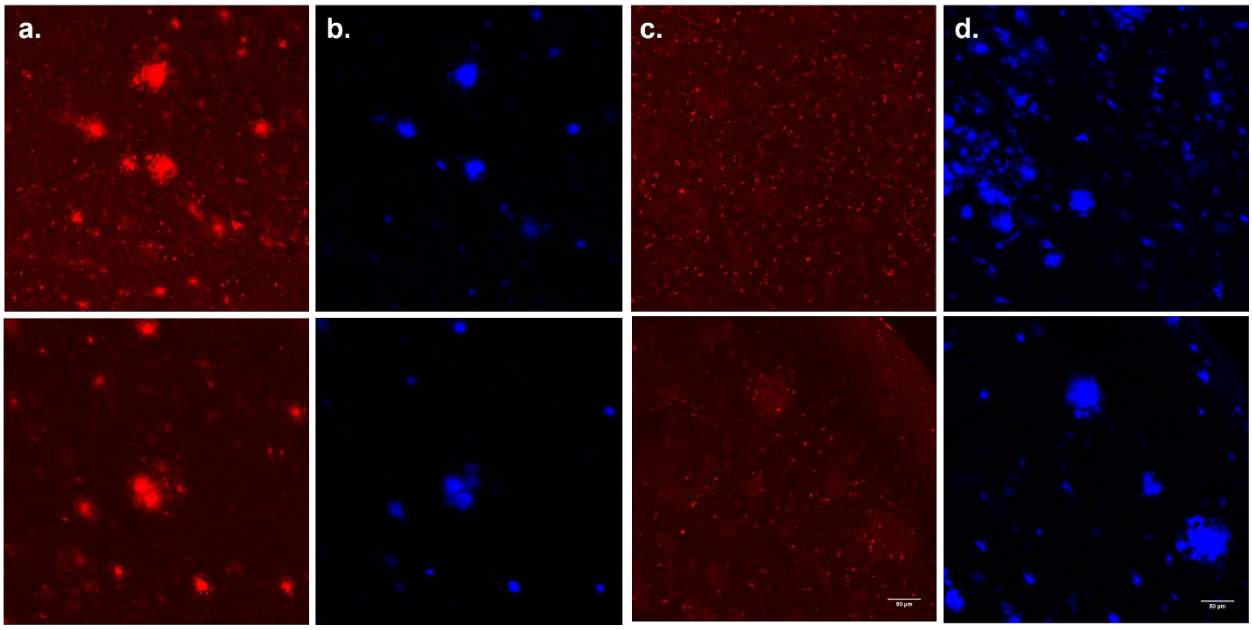

Fig. 8. Representative immunofluorescent confocal microscopy of ex vivo APP/PS1 positive mouse brain sections. 647 channel (**a.**) and X34 channel (**b.**) microscopy of the ex vivo brain sections labeled with $M1_{P96H}$-Triplet-647. 647 channel (**c.**) and X34 channel (**d.**) microscopy of the ex vivo brain sections without $M1_{P96H}$-Triplet-647 labeling.

482 the Nb3-Nb3 dimer part of $M1_{P96H}$-Triplet-647 was able to bind to amyloid plaques, with substantially

483 enhanced fluorescence signals in areas of plaques. Thus, the modest plaque labeling after intravenous

484 injection with $M1_{P96H}$-triplet-647 is not likely to be attributed to lack of plaque binding affinity.

485 Autofluorescence was relatively modest in the 647 channel in sections labeled with only X34 (**Fig. 8c-d**).

486 Because of the possibility of subconscious bias in selecting regions for imaging and to assess for more

487 subtle quantitative differences between $M1_{P96H}$-triplet-647 and H1-triplet-647 plaque labeling, we

488 performed randomized, blinded, automated analyses of the brain sections to objectively compare the

489 confocal imaging results. Eleven or twelve confocal stacks of images were acquired at randomly selected

490 x, y coordinates in cortex (**Additional file 1: Fig. S1**). Confocal images of brain sections were processed

491 using ImageJ for quantitative assessment.

492 The % area of X34 coverage, % area of Triplet-647 coverage and the % area ratio of Triplet-647/X34

493 coverage were averaged across the eleven to twelve images stacks acquired for each mouse brain. The

494 average values of % area of each mouse brain was plotted in **Fig. 9**. Comparing mouse brains injected

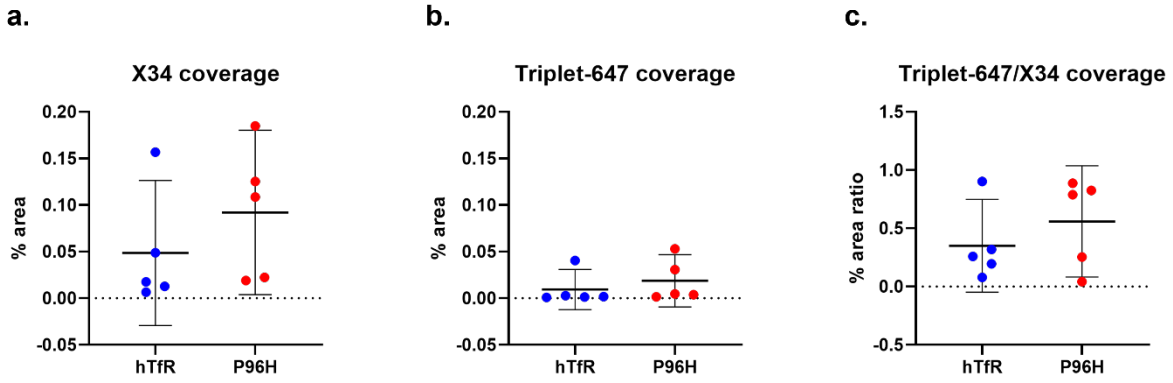

Fig. 9. % area and % area ratio of X34 channel images and 647 channel images. **a**. The % area of X34 coverage in the X34 images. There was no significant difference for mice injected with H1-triplet-647 or $M1_{P96H}$-triplet-647; unpaired student t-test, p= 0.3341 **b.** The % area of Triplet-647 coverage in 647 channel images. There was no significant difference for mice injected with H1-triplet-647 or $M1_{P96H}$-triplet-647; unpaired student t-test, p = 0.4815. **c.** The % area ratio of Triplet-647/X34 coverage. There was no significant difference for mice injected with H1-triplet-647 or $M1_{P96H}$-triplet-647; unpaired student t-test, p = 0.3788. 647 channel images and the ratio of 647 channel/X34 channel images.

495 with $M1_{P96H}$-triplet-647 or H1-triplet-647, the average values of % area of Triplet-647 coverage/% area

496 X34 coverage had no significant difference (**Fig. 9c**). There was also no significant difference for % area

497 X34 coverage or % area Triplet-647 coverage (**Fig. 9a, b**).

498 **Alternative Confocal Image Processing – thresholding and intensity measurement**

499 To ensure the finding was not affected by the specific analysis method, confocal images of brain sections
500 were analyzed in several alternative ways using ImageJ **(Additional file 1: Fig. S9**). First, X34 images were
501 alternatively thresholded at (0, 10) and (0, 30) and were converted to binary images. Because amyloid-
502 beta pathology can extend beyond the boundaries of X34 positive fibrillar plaque cores, the X34 images
503 thresholded at (0, 30) were also processed with dilation in ImageJ to add pixels from the edges of
504 plaques. These plaque and peri-plaque regions identified on the X34 images were applied to the 647
505 channel images to calculate the mean 647 signal of these regions. The mean 647 signals were averaged
506 across image stacks acquired for each mouse brain The average values of mean 647 signals of each brain
507 were plotted in **Fig. 10.** There was no significant difference of the mean 647 signal between the two

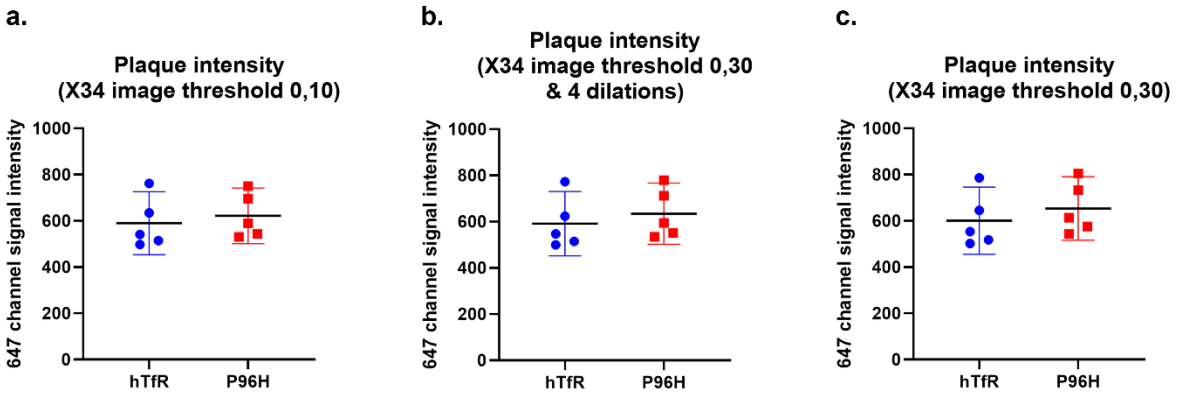

Fig. 10. Averaged mean fluorescence in the 647 channel of plaques containing regions. **a.** The threshold for X34 images was set to be at (0, 10) There was no significant difference between the mean signals from mice injected with H1-triplet-647 and mice injected with $M1_{P96H}$-triplet-647; unpaired student t-test, p = 0.6404. **b.** The threshold for X34 images was set to be at (0, 30), then the image was eroded for four times. There was no significant difference between the mean signals from mice injected with H1-triplet-647 and mice injected with $M1_{P96H}$-triplet-647; unpaired student t-test, p = 0.5527. **c.** The threshold for X34 images was set to be at (0, 30). There was no significant difference between the mean signals from mice injected with H1-triplet-647 and mice injected with $M1_{P96H}$-triplet-647; unpaired student t-test, p = 0.4829.

508 groups in any of these analyses. These findings confirmed that there was no detectible receptor
509 mediated transcytosis of $M1_{P96H}$-triplet-647 into the cortex, despite good evidence for a CNS effect for
510 the same construct when fused to neurotensin.

511 **Discussion**

512 In this study, a modular system was designed to efficiently test the ability of anti-mTfR VHHs to cross the
513 BBB using NT-induced hypothermia as a readout. Because only NT in the CNS can induce hypothermia
514 effects [34, 39, 41, 55], experimentally measured hypothermia was used to infer the VHHs' ability to
515 cross the BBB through transferrin receptor mediated transcytosis followed by VHH-NT fusion binding to
516 neurotensin receptors. Using this NT-based screening system, this study successfully identified an anti-
517 mTfR VHH variant, $M1_{P96H}$, which has good binding properties to the mouse TfR and appeared to
518 mediate BBB transport efficiently. To attempt to validate the ability of this anti-mTfR VHH to carry
519 cargos across BBB, this anti-mTfR VHH was fused with an anti-Aβ VHH dimer and fused to NT. The
520 $M1_{P96H}$-Triplet-NT retained substantial hypothermia effects after intravenous injection, confirming the
521 BBB transcytosis ability of this triplet-NT fusion. However, the modular system for VHH screening does
522 not appear to translate effectively into target binding in the cortex. To assess brain target engagement,
523 $M1_{P96H}$-triplet was conjugated to the fluorescent Alexa 647 dye and the dye conjugates were injected
524 intravenously into APP/PS1 positive transgenic mice. A similar VHH triplet dye conjugate, H1-triplet
525 which does not binding mTfR was used as a control. Surprisingly, there was no significant difference of
526 the amyloid plaque binding between these two VHH triplet dye conjugates. This result was not likely due
527 to failure of plaque binding, because the VHH triplet dye conjugates bound plaques well in *ex vivo*
528 experiments. Thus, the likely explanation for our findings was that the VHH triplet dye conjugates did
529 not effectively cross the BBB in the cortex; the hypothermia effect induced by NT did not correspond to
530 target engagement in cortex. The finding indicates that the use of NT as a rapid screening platform for
531 anti-mTfR VHHs does not necessarily predict generalized cargo delivery across the BBB.
532
533 The lack of correspondence between NT induced hypothermia after intravenous injection and brain
534 target engagement could be possibly explained by the concept that the BBB is not a unitary
535 phenomenon, and the permeability of BBB may be different from brain region to brain region. The

536 hypothalamus is the center for thermoregulation, and likely to be the site of action of NT in the brain.
537 The preoptic area of hypothalamus contains microcircuitry through which cutaneous and core thermal
538 signals are integrated for thermoregulation and temperature homeostasis [56, 57]. Studies have found
539 that the interface between the median eminence and the arcuate nucleus of the hypothalamus is
540 somewhat leaky to molecules in the circulation [58, 59]. Cheunsuang et al. confirmed the specialized
541 nature of median eminence and medial arcuate nucleus BBB by testing the distribution of
542 hydroxystilbamidine and wheat germ agglutinin after intravenous injection [58]. They found that
543 hydroxystilbamidine was taken into the median eminence and medial part of the arcuate nucleus, while
544 the wheat germ agglutinin diffusely distributed in the arcuate nucleus and median eminence following
545 intravenous injection. Furthermore, Morita and Miyata reported the accessibility of low molecular
546 weight blood-derived molecules to the parenchyma in the median eminence and arcuate nucleus [60].
547 The hypothermia effect caused by NT binding to NT receptor is likely to be mediated in the
548 hypothalamus [39]. Young et al. explored the distribution of NT receptors in rat brains and found
549 moderate to high density of NT receptors in hypothalamus. The hypothermia effect was induced when
550 NT was injected to medial, lateral preoptic and anterior area of the hypothalamus. Thus, the dissociation
551 between robust NT-mediated hypothermia effects vs. negligible binding to amyloid plaques in cortex
552 after IV injection could be explained by a relatively leaky hypothalamic BBB. Future studies will be
553 required to directly test this possibility.
554
555 **Limitations**
556 There are several limitations of this study. First, although the $M1_{P96H}$-NT induced substantial
557 hypothermia, the kinetics of this anti-mTfR VHH variant have not been fully optimized. **Fig. 2** shows that
558 the dissociation rate of the $M1_{P96H}$ from mTfR was $1.33X10^{-4}$ which could be still too low. Based on
559 Hultqvist et al., after the VHH binds to the TfR and the complex is internalized, the VHH needs to

560 dissociate from the TfR to get released efficiently into the brain parenchyma [61]. When the dissociation
561 rate is too slow, VHHs may not unbind from the TfR and not get released into the brain parenchyma.
562 Second, it is possible that dye modification with Alexa 647 affected BBB transcytosis even though it did
563 not affect mTfR binding affinity *in vitro* (**Additional file 1: Fig S8**). Alternative labeling strategies will
564 need to be tested in future experiments. Reduction in autofluorescence due to lipofuscin [62] may also
565 improve the sensitivity of fluorescent dye-based detection methods. Third, the APP/PS1 mice used in
566 the study can also develop astrogliosis [63]. It is possible that the astrogliosis around the plaques could
567 impair BBB transcytosis. Fourth, we do not know the mTfR binding epitope of M1, though it does not
568 appear to interfere with transferrin binding (not shown). Also, it is formally possible, though unlikely,
569 that older APP/PS1 transgenic mice have a less permeable BBB than young WT mice; we have not
570 directly tested hypothermia effects in older APP/PS1 mice. A minor limitation is that the temperature
571 measurement was conducted using an infrared thermometer. Although belly fur was removed to
572 decrease variation and increase the accuracy and precision of temperature measurement, the use of
573 infrared thermometer to measure belly temperature still introduces inter- and intra- user error. Also,
574 the mice need to be anesthetized for acquisition of a steady temperature using the thermometer.
575 Although we kept the anesthesia time short (about 20 sec) each time to minimize the influence of
576 anesthesia on mouse body temperature. The use of anesthesia still introduced extra variations. Other
577 temperature measurement methods such as the use of implanted thermometers which provide real-
578 time temperature readings and eliminate interference with mice should be considered for future
579 experiments. Finally, we acknowledge that only one brain section posterior to bregma was analyzed for
580 each mouse. More brain sections for each mouse which cover additional brain areas, including
581 hypothalamus, will need to be imaged and analyzed in the future.
582
583 **Future directions**

584 There are many important future directions for this line of investigation. We are in the process of
585 screening other VHH variants for anti-mTfR and anti hTfR-mediated BBB transcytosis. Because the NT
586 induced hypothermia effect does not correspond to target engagement of targets in other brain areas
587 like cortex, an alternative, efficient approach to assess BBB transcytosis is needed. To allow high
588 throughput testing and prediction of therapeutic and diagnostic agent delivery to the CNS, *in vitro* BBB
589 models have been used. Cecchelli et al. developed a human *in vitro* BBB model using cord blood-derived
590 hematopoietic stem cells [64]. This model shows good correlation between *in vitro* predicted ratio of
591 unbound drug concentration in brain and *in vivo* ratio reported in humans. Shayan et al. made a murine
592 *in vitro* BBB model using murine brain microvascular endothelial cells which also shows good correlation
593 of compound permeability compared with *in vivo* values [65]. However, these *in vitro* models do not
594 always reflect the *in vivo* BBB function. Garberg et al. evaluated multiple different *in vitro* models in
595 comparison with an *in vivo* mouse brain uptake assay to understand the *in vitro* models' potential to
596 predict *in vivo* transport of compounds across BBB [66]. Low correlations between *in vitro* and *in vivo*
597 data were obtained with a total of twenty-two compounds. Because of the complexity of the *in vivo*
598 environment, *in vitro* BBB models were not recommended to be used in isolation to assess target
599 engagement in brain [67]. There are many other methods to assess BBB transcytosis. For example,
600 Stocki et al. tested the BBB transcytosis of a variable domain of new antigen receptors (VNAR) TXB2 by
601 fractionating capillaries from the brain parenchyma and measured the concentration in capillaries and
602 brain parenchyma [34]. Yu et al. assessed the uptake of an anti-TfR antibody by homogenizing the brain
603 target areas and measuring the antibody concentration with ELISA [17]. A new screening platform will
604 need to be established and tested in the future to facilitate of the discovery of optimal anti-mTfR VHHs.
605
606 There were no apparent safety concerns raised during the experiments reported here, but the safety
607 profile of the VHHs will be formally assessed in the future to make sure that the binding of VHHs to the

608 mTfR does not interfere with physiological iron uptake and that the foreign protein constructs do not
609 cause major immunological responses or other toxicities.
610
611 In addition, extension of VHH fusion protein half-life in the circulation may improve BBB transcytosis.
612 The half-life of single VHHs and VHH triplets was measured to be 2-3 minutes in the mouse after IV
613 injection [68]. The lack of differences in brain signal may be caused by the fast clearance of the VHHs,
614 which did not allow enough VHHs to bind to the TfR on the brain endothelial cells. Conjugation of the
615 VHHs to albumin binding domains, immunoglobulin Fc domains or PEG to prolong VHH' half-lives will be
616 tested in the future [69-71].
617
618 While not directly related to the main aims of the project involving development of brain MRI molecular
619 contrast agents, the mechanisms underlying potential differences in BBB function in the hypothalamus
620 vs. cortex are worthy of further investigation. To begin, target engagement of the Triplet-647 in
621 hypothalamus will need to be assessed. The hypothalamus area of the brain sections will be imaged with
622 confocal microscope and analyzed using ImageJ. Then, the $M1_{P96H}$ could be conjugated to nanobodies
623 against another widely distributed endogenous target such as the ATP-gated ion channel P2X7, which is
624 widely distributed throughout the brain [72]. $M1_{P96H}$-anti P2X7 VHH fusion would then be intravenously
625 injected to mice and its target engagement in cortex and hypothalamus would be assessed and
626 compared. Furthermore, different sizes of dextrans could be intravenously injected to the mice to
627 understand the BBB penetration capacity in hypothalamus and other brain regions [60].
628
629 The ultimate goal of this study is to develop a family of molecular MRI contrast agents for diagnosis and
630 assessment of neurodegenerative diseases. Misdiagnosis of neurodegenerative diseases is common
631 because of their heterogeneous nature [73]. Early diagnosis of neurodegenerative diseases could help

632 with early treatments and delay hospitalization, and accurate identification of target populations could
633 help with the development of new treatments [73, 74]. MRI has been widely used for imaging
634 neurodegenerative diseases; however, structural MRI provides indirect and nonspecific measurements.
635 Neurodegenerative diseases are characterized by abnormal accumulation of misfolded proteins
636 including α-synuclein, tau, TDP-43 and Huntingtin in the CNS. Novel families of MRI contrast agents with
637 VHH and IONPs would allow visualization of pathologically specific biomarkers in the living human brain:
638 each VHH would bind to the misfolded proteins while the IONPs provide T1 MRI signals. We have
639 characterized the *in vivo* pharmacokinetics of the contrast agent and optimized the MRI sequence for
640 MR T1 imaging [68, 75], but have not optimized BBB transcytosis of contrast agents. IONPs have been
641 widely in a research context as MRI molecular contrast agents but are not typically used in clinical
642 practice. Liu et al., developed an oligomer-specific scFv antibody W20 conjugated superparamagnetic
643 iron oxide nanoparticles which specifically bound to oligomers in transgenic mouse models of
644 Parkinson's disease or Huntington's disease and provided MRI signals [76]. Sillerud et al. synthesized an
645 anti-AβPP conjugated superparamagnetic iron oxide nanoparticle for MRI detection of amyloid plaques
646 in AD [77]. However, none of these contrast agents have provided optimal BBB penetration to allow high
647 quality *in vivo* imaging. The ability of molecular contrast agents to cross the BBB and bind to brain
648 targets in sufficient quantity to give conspicuous MRI signals will need be tested with *in vivo* MR imaging
649 in the future.
650
651
652 **Conclusions**
653
654 This study used a NT based modular system to screen anti-mTfR VHHs for transferrin receptor mediated
655 transcytosis across BBB. A M1 variant, $M1_{P96H}$, was identified with good performance in inducing

656 hypothermia, an effect which requires crossing the BBB. This M1 variant was fused to the anti-Aβ VHH
657 dimer and labeled with Alexa 647. Surprisingly, however, the dye labelled VHH did not show detectible
658 labeling of amyloid plaques compared with controls after intravenous injection into transgenic mice.
659 Other methods assessing VHH BBB transcytosis will need to be developed for screening VHHs to
660 facilitate the development of MRI molecular contrast agents.

661
662
663 **List of abbreviations**

664 VHH: Singlet domain antibodies

665 BBB: Blood brain barrier

666 RMT: receptor-mediated transcytosis

667 TfR: transferrin receptor

668 mTfR: mouse transferrin receptor

669 Aβ: Amyloid-β,

670 AD: Alzheimer's Disease,

671 NT: neurotensin

672 CNS: central nervous system

673 IV: intravenous

674 HCAbs: heavy chain-only antibodies

675 scFv: single chain variable fragment

676 PBMC: peripheral blood mononuclear cell

677 cDNA: complimentary DNA

678 RIA: radioimmunoassay

679 PBS: Phosphate Buffered Saline

680 IPTG: isopropyl-beta-D-thiogalactoside

681 BSA: bovine serum albumin

682 BLI: Bio-layer interferometry

683
684
685 **Acknowledgements**

686 This research was supported by the Intramural Research Program of the NIH, NINDS. We thank Dr. Alan
687 Koretsky for providing a supportive intellectual environment. We thank the NHLBI Biophysics Core
688 Facility for the use of BLI instrument. We thank the NINDS Light Imaging Facility for use of the confocal
689 microscope. We thank Elvira Rodionova and Caroline Francescutti for expressing the VHHs. We thank Dr.
690 Yoshimi Enose-Akahata for assistance with the blinded experiment. The first author would like to thank
691 her PhD thesis committee, Dr. Philip Bayly, Dr. Dennis Barbour, Dr. Hongyu An and Dr. Vijay Sharma for
692 insightful suggestions.

693

694 **Disclaimer**

695 The authors have no conflicts of interest to disclose. The views, information or content, and conclusions
696 presented do not necessarily represent the official position or policy, nor should any official
697 endorsement be inferred, on the part of the National Institutes of Health, the Uniformed Services

University, the Department of Defense, Henry M. Jackson Foundation for the Advancement of Military Medicine, Inc., or other government agency.

Competing Interest

None.

Funding

National Institute of Neurological Disorders and Stroke (NINDS) Intramural Research Program, Uniformed Services University of the Health Sciences

Consent for publication

Not applicable

Availability of data and materials

The datasets used and/or analyzed during the current study are available from the corresponding author on reasonable request.

Authors' contributions

Conceptualization of the study: DB, TE and SS; Data collection and analysis: SS and TE; Drafting and revision of manuscript: SS, TE and DB. All authors read and approved the final manuscript.

Ethics approval and consent to participate

All animal experiments were conducted under protocols approved by the National Institute of Neurological Disorders and Stroke (NINDS)/ National Institute on Deafness and Other Communication

717 Disorders (NIDCD) Animal Care and Use Committee in the National Institutes of Health (NIH) clinical
718 center under protocol number: 1406-21.

719
720
721 **Additional file 1: Figure S1.** Schematic graph for the manual unbiased random selection method for
722 confocal image acquisition. This schematic graph shows the logic of picking coordinates for confocal
723 images acquisition. The right hemisphere of the brain was equally divided into ten parts in both x and y
724 directions. (x, y) coordinates were randomly generated using a random number generator. The
725 microscope stage was moved to the target (x, y) coordinates using the stage rulings. When (x, y)
726 coordinates fell into the areas of cortex, images were taken and cropped to include only cortical areas.
727 When (x, y) coordinates fell out of the cortex the coordinates were discarded and no images were taken.
728 Source of the mouse brain: biorender.com. **Figure S2.** The hypothermia effect of M1WT-NT before and
729 after endotoxin removal. Endotoxin removal from in M1WT-NT preparations from E. coli decreased
730 hypothermia effects at time 30min, 1hr and 1.5hr after IV injection of the M1 WT -NT (n= 3 per group).
731 The maximum hypothermic effect of 600nmol/kg body weight of M1 WT -NT was approximately 2C° less
732 after endotoxin removal. **Figure S3.** Post purification assessment of the five VHH-NT fusions M1WT-NT,
733 M1P96H-NT, M1AA-NT, M1R100dH-NT and H1-NT The purity of the monomer VHH by (a) SDS-PAGE gel
734 and exemplar (b) size-exclusion chromatography over a Superdex75 column for M1WT-NT indicating
735 >95% purity and homogeneity of the material. **Figure S4.** Post purification assessment of M1P96H-
736 triplet-NT. The purity of the triplet VHH by (a.) SDS-PAGE gel and exemplar (b.) size-exclusion
737 chromatography over a Superdex75 column for M1P96H-Triplet-NT indicating >95% purity and
738 homogeneity of the material. **Figure S5.** Histidine mutations impart a pH dependent dissociation effect
739 in M1 VHH variants. M1 variants (a.) M1WT, (b.) M1P96H and (c.) M1R100dH were incubated on mTfR
740 coated ELISA plates, followed by a stringent wash with 1x PBS buffer at pH 7.2 or pH 5.5. Following pH
741 dependent washing, the bound VHH was detected with an anti-alpaca-peroxidase antibody and the

742 reaction terminated by addition of 1M HCl. Error bars represent the standard deviation of the mean
743 values at each data point. **Figure S6.** Lack of hypothermic effect with mTfR non-binding VHH-NT fusions.
744 M1AA-NT and H1-NT were injected at doses of 1400nmol/kg body weight. M1AA-NT and H1-NT lack
745 prominent hypothermia effects (n=3 per group). **Figure S7.** Affinity binding curves of M1P96H-triplet-NT
746 and H1-triplet-NT binding affinity (KD) to mTfR and Aβ. Using biolayer interferometry on a Octet Red96
747 system, association and dissociation rates were determined by immobilizing biotinylated VHH (a, c) or
748 biotinylated amyloid beta (b, d) onto streptavidin-coated optical sensors. M1P96H-triplet-NT
749 association and dissociation curve to (a) mTfR and (b) Aβ. The affinity of M1P96H-triplet-NTwas
750 measured to be 1.63nM to mTfR and 9.98nM to Aβ. H1-triplet-NT association and dissociation curve to
751 (c) mTfR and (d) Aβ. The affinity of H1-triplet-NT was measured to be 9.44nM to Aβ and no binding to
752 mTfR. (n.b. = no binding). **Figure S8.** mTfR ELISA on M1P96H-Triplet before and after 647 labelling. VHH
753 was incubated with mTfR absorbed to ELISA plates and detected using an anti-alpaca-peroxidase
754 antibody to determine the impact of fluorophore conjugation. The near overlapping binding curves
755 indicate a lack of effect following fluorophore labelling. Error bars represent the standard deviation of
756 the mean values at each data point. **Figure S9.** Quantitative analysis procedure for confocal images with
757 thresholding followed by automated plaque selection and mean 647 channel signal calculation. An
758 APP/PS1 positive naïve brain slice with ex vivo M1P96H-Triplet-647 labeling was used as the example.
759 Column a. shows a representative confocal microscope image of cortex X34 staining. Column b. shows
760 the X34 labeled images after thresholding. Column c. shows automated selection of regions of plaques
761 based on the thresholded images. Column d. shows the application of selected areas (from thresholded
762 X34 images) to the 647 channel images.

763

764
765
766

767 **References**

768 1. LaFerla FM, Oddo S. Alzheimer's disease: Abeta, tau and synaptic dysfunction. Trends Mol Med.
769 2005;11:170-6. doi: 10.1016/j.molmed.2005.02.009.
770 2. The Alzheimer's Association. 2021 Alzheimer's disease facts and figures. Alzheimers Dement.
771 2021;17:327-406. doi: 10.1002/alz.12328.
772 3. Graham WV, Bonito-Oliva A, Sakmar TP. Update on Alzheimer's Disease Therapy and Prevention
773 Strategies. Annu Rev Med. 2017;68:413-30. doi: 10.1146/annurev-med-042915-103753.
774 4. Takizawa C, Thompson PL, van Walsem A, Faure C, Maier WC. Epidemiological and economic
775 burden of Alzheimer's disease: a systematic literature review of data across Europe and the United
776 States of America. J Alzheimers Dis. 2015;43:1271-84. doi: 10.3233/jad-141134.
777 5. Risacher SL, Saykin AJ. Neuroimaging and other biomarkers for Alzheimer's disease: the
778 changing landscape of early detection. Annu Rev Clin Psychol. 2013;9:621-48. doi: 10.1146/annurev-
779 clinpsy-050212-185535.
780 6. Clark CM, Davatzikos C, Borthakur A, Newberg A, Leight S, Lee VM, et al. Biomarkers for early
781 detection of Alzheimer pathology. Neurosignals. 2008;16:11-8. doi: 10.1159/000109754.
782 7. Beach TG, Monsell SE, Phillips LE, Kukull W. Accuracy of the clinical diagnosis of Alzheimer
783 disease at National Institute on Aging Alzheimer Disease Centers, 2005-2010. J Neuropathol Exp Neurol.
784 2012;71:266-73. doi: 10.1097/NEN.0b013e31824b211b.
785 8. Wurtman R. Biomarkers in the diagnosis and management of Alzheimer's disease. Metabolism.
786 2015;64:S47-50. doi: 10.1016/j.metabol.2014.10.034.
787 9. ten Kate M, Redolfi A, Peira E, Bos I, Vos SJ, Vandenberghe R, et al. MRI predictors of amyloid
788 pathology: results from the EMIF-AD Multimodal Biomarker Discovery study. Alzheimer's Research &
789 Therapy. 2018;10:100. doi: 10.1186/s13195-018-0428-1.
790 10. Morris E, Chalkidou A, Hammers A, Peacock J, Summers J, Keevil S. Diagnostic accuracy of 18F
791 amyloid PET tracers for the diagnosis of Alzheimer's disease: a systematic review and meta-analysis.
792 European Journal of Nuclear Medicine and Molecular Imaging. 2016;43:374-85. doi: 10.1007/s00259-
793 015-3228-x.
794 11. Lee G, Dallas S, Hong M, Bendayan R. Drug transporters in the central nervous system: brain
795 barriers and brain parenchyma considerations. Pharmacol Rev. 2001;53:569-96.
796 12. Pardridge WM. Drug and gene targeting to the brain with molecular Trojan horses. Nat Rev Drug
797 Discov. 2002;1:131-9. doi: 10.1038/nrd725.
798 13. Oller-Salvia B, Sánchez-Navarro M, Giralt E, Teixidó M. Blood-brain barrier shuttle peptides: an
799 emerging paradigm for brain delivery. Chem Soc Rev. 2016;45:4690-707. doi: 10.1039/c6cs00076b.
800 14. Malakoutikhah M, Teixidó M, Giralt E. Shuttle-mediated drug delivery to the brain. Angew Chem
801 Int Ed Engl. 2011;50:7998-8014. doi: 10.1002/anie.201006565.
802 15. Bien-Ly N, Yu YJ, Bumbaca D, Elstrott J, Boswell CA, Zhang Y, et al. Transferrin receptor (TfR)
803 trafficking determines brain uptake of TfR antibody affinity variants. J Exp Med. 2014;211:233-44. doi:
804 10.1084/jem.20131660.
805 16. Gupta Y, Jain A, Jain SK. Transferrin-conjugated solid lipid nanoparticles for enhanced delivery of
806 quinine dihydrochloride to the brain. J Pharm Pharmacol. 2007;59:935-40. doi: 10.1211/jpp.59.7.0004.
807 17. Yu YJ, Zhang Y, Kenrick M, Hoyte K, Luk W, Lu Y, et al. Boosting brain uptake of a therapeutic
808 antibody by reducing its affinity for a transcytosis target. Sci Transl Med. 2011;3:84ra44. doi:
809 10.1126/scitranslmed.3002230.
810 18. Wiley DT, Webster P, Gale A, Davis ME. Transcytosis and brain uptake of transferrin-containing
811 nanoparticles by tuning avidity to transferrin receptor. Proc Natl Acad Sci U S A. 2013;110:8662-7. doi:
812 10.1073/pnas.1307152110.

813 19. Jefferies WA, Brandon MR, Hunt SV, Williams AF, Gatter KC, Mason DY. Transferrin receptor on
814 endothelium of brain capillaries. Nature. 1984;312:162-3. doi: 10.1038/312162a0.
815 20. Pardridge WM, Buciak JL, Friden PM. Selective transport of an anti-transferrin receptor antibody
816 through the blood-brain barrier in vivo. J Pharmacol Exp Ther. 1991;259:66-70.
817 21. Hamers-Casterman C, Atarhouch T, Muyldermans S, Robinson G, Hamers C, Songa EB, et al.
818 Naturally occurring antibodies devoid of light chains. Nature. 1993;363:446-8. doi: 10.1038/363446a0.
819 22. Hassanzadeh-Ghassabeh G, Devoogdt N, De Pauw P, Vincke C, Muyldermans S. Nanobodies and
820 their potential applications. Nanomedicine (Lond). 2013;8:1013-26. doi: 10.2217/nnm.13.86.
821 23. Harmsen MM, De Haard HJ. Properties, production, and applications of camelid single-domain
822 antibody fragments. Appl Microbiol Biotechnol. 2007;77:13-22. doi: 10.1007/s00253-007-1142-2.
823 24. van der Linden RH, Frenken LG, de Geus B, Harmsen MM, Ruuls RC, Stok W, et al. Comparison of
824 physical chemical properties of llama VHH antibody fragments and mouse monoclonal antibodies.
825 Biochim Biophys Acta. 1999;1431:37-46. doi: 10.1016/s0167-4838(99)00030-8.
826 25. Oliveira S, van Dongen GA, Stigter-van Walsum M, Roovers RC, Stam JC, Mali W, et al. Rapid
827 visualization of human tumor xenografts through optical imaging with a near-infrared fluorescent anti-
828 epidermal growth factor receptor nanobody. Mol Imaging. 2012;11:33-46.
829 26. Stijlemans B, Conrath K, Cortez-Retamozo V, Van Xong H, Wyns L, Senter P, et al. Efficient
830 targeting of conserved cryptic epitopes of infectious agents by single domain antibodies. African
831 trypanosomes as paradigm. J Biol Chem. 2004;279:1256-61. doi: 10.1074/jbc.M307341200.
832 27. Food and Drug Administration. FDA approved caplacizumab-yhdp. February 2019.
833 https://www.fda.gov/drugs/resources-information-approved-drugs/fda-approved-caplacizumab-yhdp.
834 28. Ishiwatari-Ogata C, Kyuuma M, Ogata H, Yamakawa M, Iwata K, Ochi M, et al. Ozoralizumab, a
835 Humanized Anti-TNFα NANOBODY® Compound, Exhibits Efficacy Not Only at the Onset of Arthritis in a
836 Human TNF Transgenic Mouse but Also During Secondary Failure of Administration of an Anti-TNFα IgG.
837 Frontiers in Immunology. 2022;13. doi: 10.3389/fimmu.2022.853008.
838 29. D'Huyvetter M, Vos J, Caveliers V, Vaneycken I, Heemskerk J, Duhoux FP, et al. Phase I Trial of
839 (131)I-GMIB-Anti-HER2-VHH1, a New Promising Candidate for HER2-Targeted Radionuclide Therapy in
840 Breast Cancer Patients. J Nucl Med. 2021;62:1097-105. doi: 10.2967/jnumed.120.255679.
841 30. Sheff J, Wang P, Xu P, Arbour M, Masson L, van Faassen H, et al. Defining the epitope of a
842 blood–brain barrier crossing single domain antibody specific for the type 1 insulin-like growth factor
843 receptor. Scientific Reports. 2021;11:4284. doi: 10.1038/s41598-021-83198-w.
844 31. Stanimirovic DKK, K.; Haqqani, A.S.; Sulea, T.; Arbabi-Ghahroudi, M.; Massie, B.; Gilbert, R.,
845 inventorInsulin-like growth factor 1 receptor-specific antibodies and uses thereof patent
846 US10100117B2. 2018.
847 32. Danis C, Dupré E, Zejneli O, Caillierez R, Arrial A, Bégard S, et al. Inhibition of Tau seeding by
848 targeting Tau nucleation core within neurons with a single domain antibody fragment. Mol Ther.
849 2022;30:1484-99. doi: 10.1016/j.ymthe.2022.01.009.
850 33. Dupré E, Danis C, Arrial A, Hanoulle X, Homa M, Cantrelle FX, et al. Single Domain Antibody
851 Fragments as New Tools for the Detection of Neuronal Tau Protein in Cells and in Mice Studies. ACS
852 Chem Neurosci. 2019;10:3997-4006. doi: 10.1021/acschemneuro.9b00217.
853 34. Stocki P, Szary J, Rasmussen CLM, Demydchuk M, Northall L, Logan DB, et al. Blood-brain barrier
854 transport using a high affinity, brain-selective VNAR antibody targeting transferrin receptor 1. Faseb j.
855 2021;35:e21172. doi: 10.1096/fj.202001787R.
856 35. Carraway R, Leeman SE. The isolation of a new hypotensive peptide, neurotensin, from bovine
857 hypothalami. J Biol Chem. 1973;248:6854-61.
858 36. Ratner C, Skov LJ, Raida Z, Bächler T, Bellmann-Sickert K, Le Foll C, et al. Effects of Peripheral
859 Neurotensin on Appetite Regulation and Its Role in Gastric Bypass Surgery. Endocrinology.
860 2016;157:3482-92. doi: 10.1210/en.2016-1329.

861 37. Martin GE, Bacino CB, Papp NL. Hypothermia elicited by the intracerebral microinjection of
862 neurotensin. Peptides. 1980;1:333-9. doi: 10.1016/0196-9781(80)90011-x.
863 38. Kokko KP, Hadden MK, Price KL, Orwig KS, See RE, Dix TA. In vivo behavioral effects of stable,
864 receptor-selective neurotensin[8-13] analogues that cross the blood-brain barrier. Neuropharmacology.
865 2005;48:417-25. doi: 10.1016/j.neuropharm.2004.10.008.
866 39. Young WS, 3rd, Kuhar MJ. Neurotensin receptor localization by light microscopic
867 autoradiography in rat brain. Brain Res. 1981;206:273-85. doi: 10.1016/0006-8993(81)90532-1.
868 40. Bissette G, Nemeroff CB, Loosen PT, Prange AJ, Lipton MA. Hypothermia and intolerance to cold
869 induced by intracisternal administration of the hypothalamic peptide neurotensin. Nature.
870 1976;262:607-9. doi: 10.1038/262607a0.
871 41. Wouters Y, Jaspers T, De Strooper B, Dewilde M. Identification and in vivo characterization of a
872 brain-penetrating nanobody. Fluids Barriers CNS. 2020;17:62. doi: 10.1186/s12987-020-00226-z.
873 42. Esparza TJ, Martin NP, Anderson GP, Goldman ER, Brody DL. High affinity nanobodies block
874 SARS-CoV-2 spike receptor binding domain interaction with human angiotensin converting enzyme.
875 Scientific Reports. 2020;10:22370. doi: 10.1038/s41598-020-79036-0.
876 43. Pardon E, Laeremans T, Triest S, Rasmussen SGF, Wohlkönig A, Ruf A, et al. A general protocol
877 for the generation of Nanobodies for structural biology. Nature Protocols. 2014;9:674-93. doi:
878 10.1038/nprot.2014.039.
879 44. Paraschiv G, Vincke C, Czaplewska P, Manea M, Muyldermans S, Przybylski M. Epitope structure
880 and binding affinity of single chain llama anti-β-amyloid antibodies revealed by proteolytic excision
881 affinity-mass spectrometry. J Mol Recognit. 2013;26:1-9. doi: 10.1002/jmr.2210.
882 45. Martin AC. Accessing the Kabat antibody sequence database by computer. Proteins.
883 1996;25:130-3. doi: 10.1002/(SICI)1097-0134(199605)25:1<130::AID-PROT11>3.0.CO;2-L.
884 46. Quan S, Hiniker A, Collet JF, Bardwell JC. Isolation of bacteria envelope proteins. Methods Mol
885 Biol. 2013;966:359-66. doi: 10.1007/978-1-62703-245-2_22.
886 47. Jankowsky JL, Fadale DJ, Anderson J, Xu GM, Gonzales V, Jenkins NA, et al. Mutant presenilins
887 specifically elevate the levels of the 42 residue beta-amyloid peptide in vivo: evidence for augmentation
888 of a 42-specific gamma secretase. Hum Mol Genet. 2004;13:159-70. doi: 10.1093/hmg/ddh019.
889 48. Jankowsky JL, Slunt HH, Ratovitski T, Jenkins NA, Copeland NG, Borchelt DR. Co-expression of
890 multiple transgenes in mouse CNS: a comparison of strategies. Biomol Eng. 2001;17:157-65. doi:
891 10.1016/s1389-0344(01)00067-3.
892 49. Styren SD, Hamilton RL, Styren GC, Klunk WE. X-34, a fluorescent derivative of Congo red: a
893 novel histochemical stain for Alzheimer's disease pathology. J Histochem Cytochem. 2000;48:1223-32.
894 doi: 10.1177/002215540004800906.
895 50. Mamat U, Wilke K, Bramhill D, Schromm AB, Lindner B, Kohl TA, et al. Detoxifying Escherichia
896 coli for endotoxin-free production of recombinant proteins. Microbial Cell Factories. 2015;14:57. doi:
897 10.1186/s12934-015-0241-5.
898 51. Varatharaj A, Galea I. The blood-brain barrier in systemic inflammation. Brain Behav Immun.
899 2017;60:1-12. doi: 10.1016/j.bbi.2016.03.010.
900 52. Food and Drug Administration. Bacterial Endotoxins/Pyrogens.
901 https://www.fda.gov/inspections-compliance-enforcement-and-criminal-investigations/inspection-
902 technical-guides/bacterial-endotoxinspyrogens. November 2014.
903 53. Schröter C, Günther R, Rhiel L, Becker S, Toleikis L, Doerner A, et al. A generic approach to
904 engineer antibody pH-switches using combinatorial histidine scanning libraries and yeast display. MAbs.
905 2015;7:138-51. doi: 10.4161/19420862.2014.985993.
906 54. Maeda K, Kato Y, Sugiyama Y. pH-dependent receptor/ligand dissociation as a determining
907 factor for intracellular sorting of ligands for epidermal growth factor receptors in rat hepatocytes. J
908 Control Release. 2002;82:71-82. doi: 10.1016/s0168-3659(02)00126-8.

909 55. Tyler-McMahon BM, Boules M, Richelson E. Neurotensin: peptide for the next millennium. Regul
910 Pept. 2000;93:125-36. doi: 10.1016/s0167-0115(00)00183-x.
911 56. Morrison SF. Central control of body temperature. F1000Res. 2016;5. doi:
912 10.12688/f1000research.7958.1.
913 57. Yoo S, Blackshaw S. Regulation and function of neurogenesis in the adult mammalian
914 hypothalamus. Prog Neurobiol. 2018;170:53-66. doi: 10.1016/j.pneurobio.2018.04.001.
915 58. Cheunsuang O, Stewart AL, Morris R. Differential uptake of molecules from the circulation and
916 CSF reveals regional and cellular specialisation in CNS detection of homeostatic signals. Cell and Tissue
917 Research. 2006;325:397-402. doi: 10.1007/s00441-006-0162-z.
918 59. Haddad-Tóvolli R, Dragano NRV, Ramalho AFS, Velloso LA. Development and Function of the
919 Blood-Brain Barrier in the Context of Metabolic Control. Front Neurosci. 2017;11:224. doi:
920 10.3389/fnins.2017.00224.
921 60. Morita S, Miyata S. Accessibility of low-molecular-mass molecules to the median eminence and
922 arcuate hypothalamic nucleus of adult mouse. Cell Biochem Funct. 2013;31:668-77. doi:
923 10.1002/cbf.2953.
924 61. Hultqvist G, Syvänen S, Fang XT, Lannfelt L, Sehlin D. Bivalent Brain Shuttle Increases Antibody
925 Uptake by Monovalent Binding to the Transferrin Receptor. Theranostics. 2017;7:308-18. doi:
926 10.7150/thno.17155.
927 62. Chen C, Liang Z, Zhou B, Li X, Lui C, Ip NY, et al. In Vivo Near-Infrared Two-Photon Imaging of
928 Amyloid Plaques in Deep Brain of Alzheimer's Disease Mouse Model. ACS Chem Neurosci. 2018;9:3128-
929 36. doi: 10.1021/acschemneuro.8b00306.
930 63. Kamphuis W, Mamber C, Moeton M, Kooijman L, Sluijs JA, Jansen AH, et al. GFAP isoforms in
931 adult mouse brain with a focus on neurogenic astrocytes and reactive astrogliosis in mouse models of
932 Alzheimer disease. PLoS One. 2012;7:e42823. doi: 10.1371/journal.pone.0042823.
933 64. Cecchelli R, Aday S, Sevin E, Almeida C, Culot M, Dehouck L, et al. A stable and reproducible
934 human blood-brain barrier model derived from hematopoietic stem cells. PLoS One. 2014;9:e99733. doi:
935 10.1371/journal.pone.0099733.
936 65. Shayan G, Choi YS, Shusta EV, Shuler ML, Lee KH. Murine in vitro model of the blood-brain
937 barrier for evaluating drug transport. Eur J Pharm Sci. 2011;42:148-55. doi: 10.1016/j.ejps.2010.11.005.
938 66. Garberg P, Ball M, Borg N, Cecchelli R, Fenart L, Hurst RD, et al. In vitro models for the blood-
939 brain barrier. Toxicol In Vitro. 2005;19:299-334. doi: 10.1016/j.tiv.2004.06.011.
940 67. Stanimirovic DB, Bani-Yaghoub M, Perkins M, Haqqani AS. Blood-brain barrier models: in vitro to
941 in vivo translation in preclinical development of CNS-targeting biotherapeutics. Expert Opin Drug Discov.
942 2015;10:141-55. doi: 10.1517/17460441.2015.974545.
943 68. Su S, Esparza TJ, Nguyen D, Mastrogiacomo S, Kim JH, Brody DL. Pharmacokinetics of Single
944 Domain Antibodies and Conjugated Nanoparticles Using a Hybrid near Infrared Method. Int J Mol Sci.
945 2021;22. doi: 10.3390/ijms22168695.
946 69. van Faassen H, Ryan S, Henry KA, Raphael S, Yang Q, Rossotti MA, et al. Serum albumin-binding
947 V(H) Hs with variable pH sensitivities enable tailored half-life extension of biologics. Faseb j.
948 2020;34:8155-71. doi: 10.1096/fj.201903231R.
949 70. Rotman M, Welling MM, van den Boogaard ML, Moursel LG, van der Graaf LM, van Buchem MA,
950 et al. Fusion of hIgG1-Fc to 111In-anti-amyloid single domain antibody fragment VHH-pa2H prolongs
951 blood residential time in APP/PS1 mice but does not increase brain uptake. Nucl Med Biol. 2015;42:695-
952 702. doi: 10.1016/j.nucmedbio.2015.03.003.
953 71. Li Q, Barrett A, Vijayakrishnan B, Tiberghien A, Beard R, Rickert KW, et al. Improved Inhibition of
954 Tumor Growth by Diabody-Drug Conjugates via Half-Life Extension. Bioconjug Chem. 2019;30:1232-43.
955 doi: 10.1021/acs.bioconjchem.9b00170.

956 72. Lord B, Ameriks MK, Wang Q, Fourgeaud L, Vliegen M, Verluyten W, et al. A novel radioligand
957 for the ATP-gated ion channel P2X7: [3H] JNJ-54232334. Eur J Pharmacol. 2015;765:551-9. doi:
958 10.1016/j.ejphar.2015.09.026.
959 73. Basak I, Patil KS, Alves G, Larsen JP, Møller SG. microRNAs as neuroregulators, biomarkers and
960 therapeutic agents in neurodegenerative diseases. Cell Mol Life Sci. 2016;73:811-27. doi:
961 10.1007/s00018-015-2093-x.
962 74. Koikkalainen J, Rhodius-Meester H, Tolonen A, Barkhof F, Tijms B, Lemstra AW, et al. Differential
963 diagnosis of neurodegenerative diseases using structural MRI data. Neuroimage Clin. 2016;11:435-49.
964 doi: 10.1016/j.nicl.2016.02.019.
965 75. Kim JH, Dodd S, Ye FQ, Knutsen AK, Nguyen D, Wu H, et al. Sensitive detection of extremely
966 small iron oxide nanoparticles in living mice using MP2RAGE with advanced image co-registration.
967 Scientific Reports. 2021;11:106. doi: 10.1038/s41598-020-80181-9.
968 76. Liu XG, Lu S, Liu DQ, Zhang L, Zhang LX, Yu XL, et al. ScFv-conjugated superparamagnetic iron
969 oxide nanoparticles for MRI-based diagnosis in transgenic mouse models of Parkinson's and
970 Huntington's diseases. Brain Res. 2019;1707:141-53. doi: 10.1016/j.brainres.2018.11.034.
971 77. Sillerud LO, Solberg NO, Chamberlain R, Orlando RA, Heidrich JE, Brown DC, et al. SPION-
972 enhanced magnetic resonance imaging of Alzheimer's disease plaques in AβPP/PS-1 transgenic mouse
973 brain. J Alzheimers Dis. 2013;34:349-65. doi: 10.3233/jad-121171.

974